catalysts

MDPI

Article

Structure–Acidity–Activity Correlation in Ammonia Decomposition over Al-Based Mixed-Oxide Catalysts: A Combined Surface and Kinetic Study

Mihaela Litinschi (Bilegan) [1], Rami Doukeh [1,*], Romuald Győrgy [2], Ionuț Banu [2], Alexandru Vlaicu [3], Gabriel Vasilievici [3], Sorin Georgian Moga [4], Andreea Madalina Pandele [5] and Dragos Mihael Ciuparu [1,*]

[1] Department of Petroleum Refining Engineering and Environmental Protection, Petroleum-Gas University of Ploiesti, 39 Bucharest Blvd., 100680 Ploiesti, Romania; mihaela_bilegan@yahoo.com
[2] Department of Chemical and Biochemical Engineering, National University of Science and Technology POLITEHNICA Bucharest, 060042 Bucharest, Romania; romuald.gyorgy@upb.ro (R.G.); ionut.banu@upb.ro (I.B.)
[3] National Institute for Research Development for Chemistry and Petrochemistry-ICECHIM-București, 202 Spl. Independenței, 060021 Bucharest, Romania; alexandru.vlaicu@icechim.ro (A.V.); gvasilievici@icechim.ro (G.V.)
[4] Regional Center of Research & Development for Materials, Processes and Innovative Products Dedicated to the Automotive Industry (CRC&D-AUTO), Pitesti University Centre, National University of Science and Technology POLITEHNICA Bucharest, 110040 Pitesti, Romania; sorin_georgian.moga@upb.ro
[5] Advanced Polymers Materials Group, National University of Science and Technology POLITEHNICA Bucharest, Gheorghe Polizu 1-7, 011061 Bucuresti, Romania; pandele.m.a@gmail.com
* Correspondence: rami.doukeh@upg-ploiesti.ro (R.D.); dciuparu@upg-ploiesti.ro (D.M.C.)

Abstract

Ammonia decomposition represents a promising route for CO_2-free hydrogen production; however, the development of efficient and stable catalysts remains a critical challenge. In this work, a series of Al-based mixed-oxide catalysts (AlM, where M = Ni, Co, Ce) were synthesized via co-precipitation and systematically investigated to elucidate the relationship between physicochemical properties and catalytic performance in ammonia decomposition. Comprehensive characterization by X-ray diffraction (XRD), N_2 physisorption (BET), scanning electron microscopy with energy-dispersive X-ray spectroscopy (SEM–EDX), X-ray photoelectron spectroscopy (XPS), thermogravimetric analysis (TGA), and pyridine-adsorbed Fourier transform infrared spectroscopy (FTIR-Py) revealed significant variations in surface area, morphology, dispersion, and acidity as a function of the incorporated metal. Among the investigated catalysts, the AlNi system exhibited superior activity, achieving the highest ammonia conversion over the studied temperature range. This enhanced performance is attributed to its high specific surface area, homogeneous mesoporous structure, and a balanced distribution of Lewis/Brønsted acid sites, which promote effective ammonia adsorption, activation and decomposition. Kinetic analysis further confirmed the favorable reaction pathway on AlNi, as evidenced by its lower apparent activation energy and higher pre-exponential factor compared to the other materials. The results demonstrate a clear correlation between surface acidity, textural properties, and catalytic performance, highlighting the pivotal role of AlM interactions in governing ammonia decomposition. These findings provide valuable insights for the rational design of efficient catalysts for hydrogen production from ammonia.

Keywords: Al-based mixed oxides; hydrogen production; Langmuir–Hinshelwood kinetics

Check for updates

Academic Editors: Leonarda Liotta, Kwun Nam Hui, Tianliang Lu and Lucian Baia

Received: 19 March 2026
Revised: 8 April 2026
Accepted: 21 April 2026
Published: 1 May 2026

Copyright: © 2026 by the authors. Licensee MDPI, Basel, Switzerland. This article is an open access article distributed under the terms and conditions of the Creative Commons Attribution (CC BY) license.

1. Introduction

Hydrogen (H_2) is a convenient alternative to conventional fossil-based fuels, but its high volatility and low volumetric energy density at atmospheric pressure limit its use [1,2]. To address these limitations, compressed H_2, liquefied H_2, liquid organic H_2 carriers, and ammonia (NH_3) are the main commercially used or investigated forms of hydrogen for transportation [3]. Ammonia is one of the most promising hydrogen and energy carriers, suitable for both on-site and off-site H_2 supply models; consequently, its decomposition has become an intensively studied reaction [4]. NH_3 decomposition to hydrogen is an endothermic process that requires a high reaction temperature, and complete conversion of NH_3 is thermodynamically limited owing to equilibrium constraints [5,6]. Therefore, numerous catalytic approaches have been explored to achieve high NH_3 conversion at lower temperatures, based on more readily available and sustainable materials as alternatives to Ru-based catalysts, which, to date, remain the most effective systems for ammonia decomposition [7–11].

Nickel (Ni) and Cobalt (Co) have been extensively studied as viable substitutes. According to the "volcano plot" for ammonia decomposition, the activity of these metals is governed by their nitrogen binding energy; Ni and Co offer a balanced compromise between N–H bond activation and the recombinative desorption of N_2 which is typically the rate-determining step. Recent studies indicate that the catalytic performance of transition metals can be significantly modulated by the addition of rare-earth elements like Lanthanum (La). Lanthanum acts as a structural and electronic promoter, increasing the basicity of the support and enhancing the dispersion of the active metal phase, thereby preventing sintering at the high temperatures required for the reaction.

Efforts to refine the non-noble-based catalytic systems for NH_3 decomposition have centered on the precise management of active species and their concentration [12–14], particle size and metal–support interactions [15–17], and the electronic tuning of their surface properties in order to accelerate the overall reaction kinetics [18–20]. In this study, catalysts based on the Al-Co, Al-Ni, and Al-La systems were synthesized via coprecipitation. Unlike the traditional impregnation method, coprecipitation allows for atomic-level mixing of the precursors, leading to superior homogeneity, the formation of spinel-like structures, which can be reduced to form highly dispersed and stable metal nanoparticles, and enhanced thermal resistance, crucial for the operating temperature window of ammonia decomposition.

In this context, non-precious metal catalysts based on Ni, Co, Ce, and Fe supported on oxides, or doped with heteroatoms, have attracted significant attention due to enhanced metal–support interactions and the presence of oxygen vacancies. Among these candidates, cobalt represents an attractive alternative, from both economic and availability perspectives, for replacing ruthenium in ammonia decomposition catalysts.

Hesam Maleki and Volfango Bertola [21] reported that a self-assembled mesoporous Co–Ce–Al–O catalyst with a Co:Ce:Al molar ratio of 0.5:0.1:0.4 achieved up to 98% ammonia conversion at 550 °C under a GHSV of 12,000 $mL \cdot h^{-1} \cdot g_{cat}{}^{-1}$, while maintaining high thermal stability over 48 h. Similarly, in the 350–500 °C temperature range, NH_3 conversion over Ni/Al_2O_3-based catalysts increases with support basicity (Ni/Mg–Al–O < Ni/Ca–Al–O < Ni/Sr–Al–O < Ni/Ba–Al–O), reaching 54.1% at 500 °C for Ni/Ba–Al–O compared to 18.4% for Ni/Mg–Al–O [22].

In addition to support basicity effects, Ce-based perovskite catalysts ($CeXO_3$, X = Ni, Co, Fe) exhibit enhanced NH_3 decomposition activity compared to their impregnated counterparts, with $CeNiO_3$ showing the highest ammonia conversion (≈85%) in the intermediate temperature range (≈350–500 °C), highlighting the beneficial role of the perovskite structure and oxygen-vacancy-rich Ni environments in promoting ammonia activation [23].

Furthermore, synergistic interactions arising from optimized metal–nitrogen bond strength, moderated by charge polarization in Co–Ni alloys, facilitate ammonia dissociation and nitrogen recombination. Co–Ni/Al_2O_3 achieved the highest turnover frequency (1.05 s^{-1} at 500 °C). Related studies also investigated Ni–Mg–Al hydrotalcite-derived mixed metal oxides, demonstrating that optimized nickel content and strong metal–support interactions play a key role in improving activity and stability for ammonia decomposition [24].

Kowalczyk et al. [25] further investigated the synergistic effect of cobalt and nickel coexistence and the influence of catalytic supports (MgO, Al_2O_3, and hydrotalcite-derived Mg–Al oxides), showing that bimetallic Co–Ni catalysts exhibit significantly higher activity than their monometallic counterparts. For instance, CoNi–MgO reduced the temperature required for 90% conversion by approximately 35 °C compared to Co–MgO or Ni–MgO systems.

Beyond Ni–Co systems, Zhao et al. [26] reported that FeCo bimetallic catalysts supported on a proton-conducting perovskite oxide achieved complete ammonia conversion at 600 °C (GHSV = 6000 $L \cdot kg^{-1} \cdot h^{-1}$), significantly outperforming monometallic Fe, which reached only 47.7% conversion at 550 °C. The superior activity was attributed to Fe–Co alloying, which facilitates electron transfer and enhances nitrogen desorption.

More recently, Al-promoted CeO_2–ZrO_2 mixed oxides synthesized by co-precipitation were employed as supports for Ni catalysts in ammonia decomposition. The Ni/Al–$Ce_{0.8}Zr_{0.2}O_2$ catalyst showed enhanced activity at moderate temperatures (450–550 °C), achieving complete NH_3 conversion at 580 °C, compared to 92% at 600 °C for a reference Ni/Al_2O_3 catalyst. This improvement was attributed to increased surface area and oxygen vacancies induced by aluminum addition, which promote nickel dispersion and stronger metal–support interactions [27].

Despite extensive research on non-noble metal catalysts for ammonia decomposition, the relationship between structural properties, surface acidity, and kinetic behavior in Al-based mixed oxides remains insufficiently clarified. In particular, the roles of Lewis acid sites in NH_3 activation and the Brønsted sites in subsequent N–H bond cleavage, and their correlation with mesoporosity and catalytic performance, are not yet fully understood. Therefore, this work aims to establish a clear structure–acidity–activity–kinetics relationship for the AlNi, AlCo, and AlCe catalysts synthesized by coprecipitation, combining physicochemical characterization with catalytic evaluation and kinetic modeling to validate the proposed reaction mechanism, and identify the key factors governing ammonia decomposition.

2. Results and Discussion

2.1. Catalyst Characterization Results

2.1.1. X-Ray Diffraction Analysis

X-ray diffraction analysis (Figure 1) confirms the formation of well-defined crystalline mixed-oxide phases in the AlNi, AlCo, and AlCe catalysts resulting from coprecipitation and subsequent calcination. For the AlNi catalyst, diffraction peaks located at 2θ values of 36.8°, 44.7°, and 65.4° are assigned to the (311), (400), and (440) planes of the cubic spinel $NiAl_2O_4$ phase (JCPDS No. 10-0339), in agreement with previous studies [28–33]. These reflections indicate the incorporation of Ni^{2+} cations into the alumina lattice through solid-state reactions, characteristic of spinel formation in coprecipitated systems. Additional weaker peaks observed at 43.4° and 62.9° correspond to the (200) and (220) planes of NiO, suggesting the presence of a minor segregated nickel oxide phase [34].

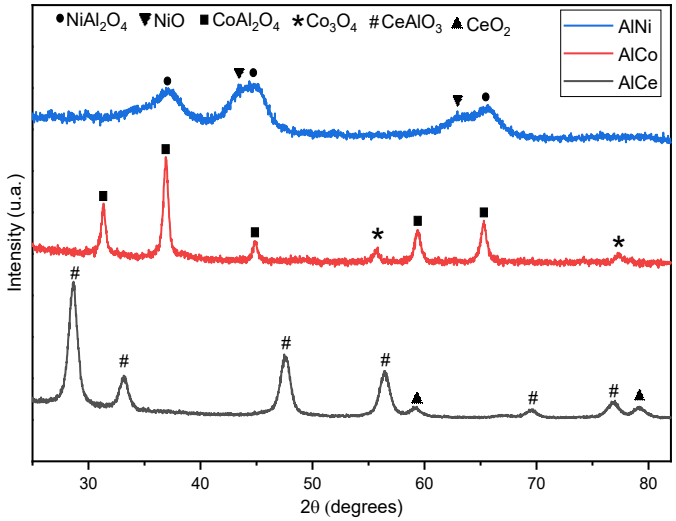


Figure 1. X-ray diffraction (XRD) patterns of the coprecipitated AlNi, AlCo, and AlCe mixed-oxide catalysts.

The AlCo catalyst exhibits characteristic reflections at 2θ = 31.3°, 36.8°, 44.8°, 59.4°, and 65.3°, which can be indexed to the (220), (311), (400), (511), and (440) planes of the $CoAl_2O_4$ spinel structure (JCPDS No. 44-0160) [33,35–38]. This phase formation reflects the homogeneous integration of cobalt ions into the alumina framework during coprecipitation. Minor diffraction peaks at 2θ = 55.8° (422) and 77.4° (533) are attributed to Co_3O_4, indicating partial segregation of cobalt oxide [39,40].

The XRD pattern of the AlCe catalyst displays intense and well-defined peaks at 2θ ≈ 28.6°, 33.3°, 47.6°, 56.5°, 69.9°, and 77.2°, corresponding to the (002), (110), (111), (220), (210), and (211) planes of $CeAlO_3$ (JCPDS No. 48-1548) [41–45]. Additional reflections at approximately 59.2° and 79° are assigned to the (222) and (331) planes of CeO_2 [46], indicating the coexistence of cerium-containing oxide phases formed within the mixed-oxide matrix.

Crystallite size analysis for the three catalysts was performed using the Debye–Scherrer equation [47–49], and the calculated average values for each identified crystalline phase are summarized in Table 1.

For the AlNi catalyst, the $NiAl_2O_4$ spinel phase exhibits an average crystallite size of 2.86 nm, whereas the segregated NiO phase shows a slightly larger value of 5.46 nm. This indicates a high degree of dispersion of the spinel phase within the alumina matrix, which is expected to enhance the accessibility and density of active sites.

In contrast, the AlCo catalyst shows significantly larger crystallite sizes, with $CoAl_2O_4$ and Co_3O_4 phases displaying average values of 14.55 nm and 15.27 nm, respectively. This larger crystallite size range suggests a higher degree of crystallinity and particle growth during calcination, which may lead to reduced surface dispersion and, consequently, a lower number of accessible active sites.

For the AlCe catalyst, intermediate crystallite sizes are observed, with $CeAlO_3$ and CeO_2 phases exhibiting average values of 8.59 nm and 8.44 nm, respectively. These values indicate a moderate balance between crystallinity and dispersion, which may contribute to a more favorable combination of structural and surface properties.

A comparative evaluation reveals a clear trend in crystallite size evolution, following the order AlNi < AlCe < AlCo. The smaller crystallites observed for AlNi indicate enhanced structural dispersion, whereas the larger crystallites in AlCo reflect pronounced particle coalescence and crystal growth.

Table 1. XRD-derived crystallite size and phase identification of Al-based catalysts.

Catalyst	Phase	FWHM	(hkl)	2θ (°)	D (nm)	Average D (nm)
AlNi	$NiAl_2O_4$	5.83	(311)	36.8	1.45	2.86
		2.32	(400)	44.7	3.74	
		2.75	(440)	65.4	3.47	
	NiO	1.57	(200)	43.4	5.50	5.46
		1.74	(220)	62.9	5.41	
AlCo	$CoAl_2O_4$	0.56	(220)	31.3	15.02	14.55
		0.56	(311)	36.8	15.19	
		0.64	(400)	44.8	13.67	
		0.64	(511)	59.4	14.45	
		0.66	(440)	65.3	14.44	
	Co_3O_4	0.54	(422)	55.8	16.88	15.27
		0.75	(533)	77.4	13.65	
AlCe	$CeAlO_3$	1.00	(002)	28.6	8.28	8.59
		1.09	(110)	33.3	7.71	
		1.05	(220)	47.6	8.35	
		1.08	(200)	56.5	8.44	
		1.00	(210)	69.9	9.74	
		1.14	(211)	77.2	9.00	
	CeO_2	1.11	(222)	59.2	8.32	8.44
		1.22	(331)	79	8.55	

Overall, the variation in crystallite size among the synthesized catalysts is expected to play a key role in determining catalytic performance, as smaller crystallites provide a higher surface-to-volume ratio, promoting improved adsorption and activation of reactant molecules. This parameter, together with phase composition and surface acidity, governs the overall catalytic efficiency in ammonia decomposition.

2.1.2. X-Ray Photoelectron Spectroscopy (XPS) Analysis

The surface chemical states of the synthesized AlNi, AlCo, and AlCe mixed-oxide catalysts were examined by X-ray photoelectron spectroscopy. All spectra were calibrated using the C 1s signal at 284.8 eV to correct for possible surface charging effects. The corresponding survey spectra are presented in Figure 2, while the high-resolution spectra for aluminum and oxygen—elements existing in all synthesized catalysts—are presented in Figure 3.

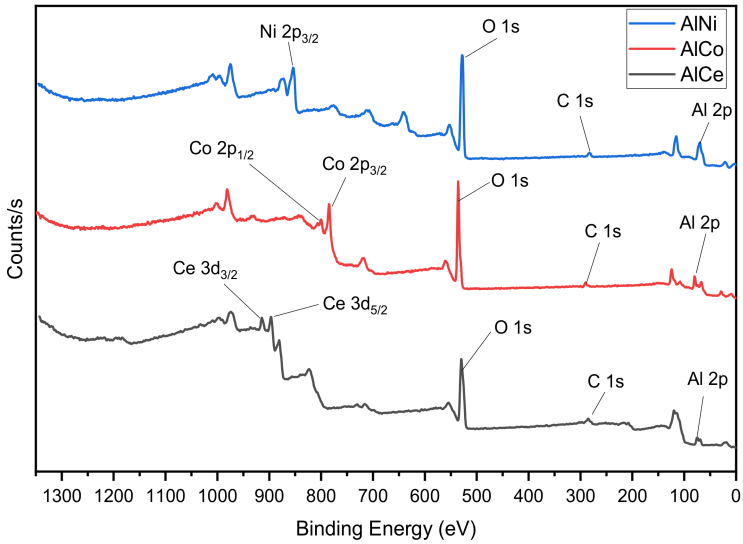


Figure 2. Survey XPS spectra of AlNi, AlCo, and AlCe catalysts.

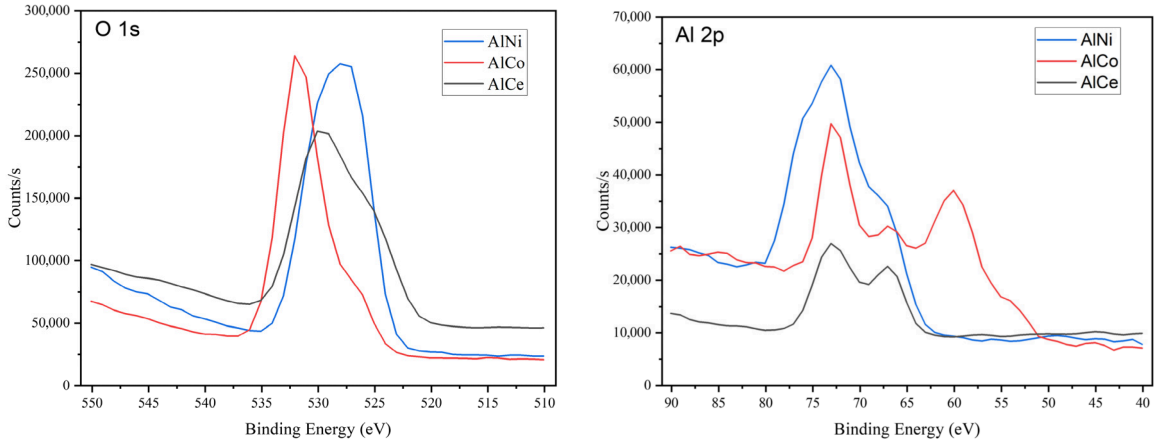


Figure 3. High-resolution XPS spectra of the O 1s and Al 2p regions of synthesized catalysts.

The survey spectra illustrate the characteristic core-level signals of Al, Ni, Co, Ce, O, and C for the three materials. The Al 2p signal appears in the range of ~72–73 eV (Figure 2), close to the reported Al^{3+} binding energy (~74.3 eV) in spinel-type aluminates such as $NiAl_2O_4$, $CoAl_2O_4$ and $CeAlO_3$ [50–55], confirming the incorporation of Al^{3+} into the oxide lattice.

For AlNi, the characteristic Ni $2p_{3/2}$ and Ni $2p_{1/2}$ peaks located at ~855–856 eV and ~873 eV, respectively, are consistent with Ni^{2+} species in a spinel environment. The binding energy of Ni $2p_{3/2}$ agrees well with reported values for $NiAl_2O_4$ [50,51,56,57], confirming the formation of a nickel aluminate phase. This observation is fully consistent with the XRD results, where $NiAl_2O_4$ was identified as the dominant crystalline phase.

In the case of AlCo, the Co 2p spectrum exhibits Co $2p_{3/2}$ and Co $2p_{1/2}$ features around ~786 and ~803 eV (Figure 2), characteristic of high-spin Co^{2+} species in $CoAl_2O_4$ [52,53,58,59]. No distinct peak near ~780 eV, typically associated with Co_3O_4 [60], is clearly resolved in the surface-sensitive XPS spectrum. The minor Co_3O_4 reflections detected by XRD may therefore correspond to trace bulk phases present below the XPS detection limit or predominantly located beneath the outermost surface layers.

For AlCe, the Ce 3d region displays characteristic multiplet features, with the main contributions observed at approximately 895 eV (Ce $3d_{5/2}$) and 914 eV (Ce $3d_{3/2}$), corresponding to mixed Ce^{3+}/Ce^{4+} oxidation states typical of cerium-containing oxide systems [55,61].

The presence of Ce^{3+} is generally associated with $CeAlO_3$-type environments, while Ce^{4+} corresponds to CeO_2 species. Due to the intrinsic multiplet splitting and complex final-state effects characteristic of the Ce 3d region, the analysis is presented qualitatively in terms of mixed valence states. The spectral profile is consistent with the coexistence of $CeAlO_3$ and minor CeO_2 phases identified by XRD, although the CeO_2 contribution appears limited, in agreement with its low relative intensity in the diffraction pattern.

The O 1s spectra (≈529–533 eV) can be deconvoluted into lattice oxygen components associated with metal–oxygen bonds (Ni–O–Al, Co–O–Al, Ce–O–Al) and higher-binding-energy contributions assigned to surface hydroxyl or defect-related oxygen species [52,58,62,63]. The relative intensity of these components reflects differences in local coordination environments and defect density among the three catalysts. These observations confirm that the bulk crystalline phases identified by XRD are also reflected in the near-surface chemical states detected by XPS.

The O 1s high-resolution spectra of all samples presented in Figure 3 exhibit broad, asymmetric peaks in the 529–532 eV range, indicative of multiple oxygen environments, including lattice O^{2-}, bridging Al–O–M species, and surface hydroxyl or carbonate groups [64,65]. A clear trend in binding energy is observed (AlCo > AlNi > AlCe), reflecting the electron-withdrawing strength of the secondary metal ion. Co^{3+} induces the highest binding energy due to its strong Lewis acidity, which reduces electron density around oxygen. Ni^{2+} shows an intermediate effect, consistent with its lower charge density and typical incorporation in $NiAl_2O_4$ spinel structures [66,67]. In contrast, AlCe exhibits the lowest binding energy due to the mixed valence (Ce^{3+}/Ce^{4+}) and 4f orbital participation of cerium, allowing partial back-donation of electron density to oxygen [68,69]. Peak broadening, most pronounced in AlCe, reflects increased structural disorder and diverse oxygen coordination environments caused by the large ionic radius mismatch of cerium [69,70].

The Al 2p spectra shown in Figure 3 further confirm that the aluminum electronic environment is strongly influenced by the secondary metal. Shifts in binding energy arise from two main effects, the inductive electron withdrawal through Al–O–M bridges, and changes in the Madelung potential due to differences in charge, size, and polarizability of neighboring ions [71,72]. AlNi shows a sharp, symmetric peak consistent with a well-ordered $NiAl_2O_4$ spinel, suggesting minimal lattice distortion. AlCo displays a higher binding energy and asymmetric features, attributed to the stronger electron-withdrawing nature of Co^{3+} and mixed Co^{2+}/Co^{3+} valence states causing local distortions [73,74]. AlCe presents the broadest and weakest Al 2p signal, reflecting significant lattice strain, heterogeneous coordination environments, and long-range electronic perturbations induced by Ce 4f–O 2p hybridization [68,69]. Surface segregation of cerium may also contribute to reduced Al signal intensity [75].

The combined O 1s and Al 2p results demonstrate consistent electronic trends governed by the nature of the secondary metal ion, rather than signatures of separate oxide phases. This provides strong spectroscopic evidence for true chemical integration within a shared lattice. The observed binding energy order (AlCo > AlNi > AlCe) aligns with the Lewis acidity sequence $Co^{3+} > Ni^{2+} > Ce^{3+}$ and correlates with known metal–oxygen bond ionicity trends [64,66,67,76]. Additionally, peak broadening correlates with ionic radius mismatch, highlighting lattice strain as a secondary factor influencing spectral features. However, when assessing the surface acidity, we have to factor in the three-fold larger specific surface area of the AlNi sample compared to the AlCo catalyst, as discussed below.

2.1.3. Nitrogen Adsorption–Desorption Isotherms

The nitrogen adsorption–desorption isotherms of the AlNi, AlCo, and AlCe catalysts are presented in Figure 4. All samples exhibit a gradual nitrogen uptake at low relative

pressures, followed by a pronounced increase in the adsorbed volume at higher P/P_0 values, accompanied by a clear hysteresis loop between the adsorption and desorption branches. According to the IUPAC classification, these isotherms correspond to type IV behavior, which is characteristic of mesoporous materials where capillary condensation occurs within mesopores [77,78].

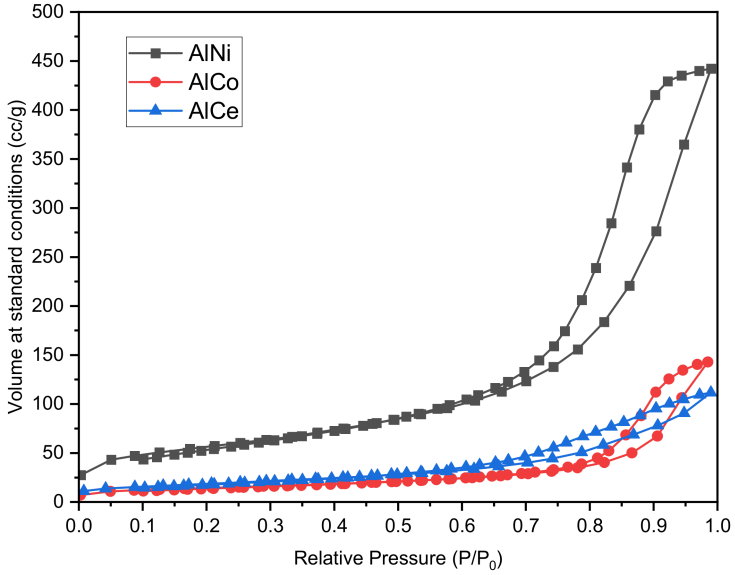


Figure 4. N_2 adsorption–desorption isotherms of aluminum-based catalysts (AlNi, AlCo, and AlCe).

At elevated relative pressures, the nitrogen adsorption increases sharply for all samples, reflecting progressive pore filling and capillary condensation phenomena. This feature indicates the presence of mesopores with contributions from larger interparticle voids and/or macroporous domains, commonly observed in oxide catalysts prepared by co-precipitation methods [79,80]. The magnitude of the adsorbed volume follows the order AlNi > AlCo > AlCe, reflecting differences in the accessible surface area and pore volume among samples.

Further insight into the pore structure is obtained from the shape of the hysteresis loops. The AlNi catalyst exhibits a pronounced and asymmetric hysteresis loop that can be classified as H2(b), suggesting the presence of pore-network effects and ink-bottle-like mesopores with pore blocking during desorption [77,78]. In contrast, the hysteresis loops of AlCo and AlCe are less developed; AlCo still shows H2(b)-type characteristics, whereas AlCe displays a more open loop approaching H3 behavior, which is typically associated with aggregates of non-rigid particles forming slit-shaped interparticle pores [77,78]. These differences indicate that AlNi possesses a more complex and constrained mesoporous network, while AlCe is dominated by interparticle slit-like porosity.

The BJH pore size distribution curves shown in Figure 5 reveal that the AlNi catalyst displays a relatively narrow and well-defined mesopore distribution centered at approximately 10–15 nm, consistent with its large pore volume and surface area. A similar, though less intense, mesopore distribution is observed for AlCo, reflecting a lower density of accessible pores. In contrast, AlCe exhibits a broader and less uniform pore size distribution shifted toward smaller mesopores, in agreement with its reduced pore volume.

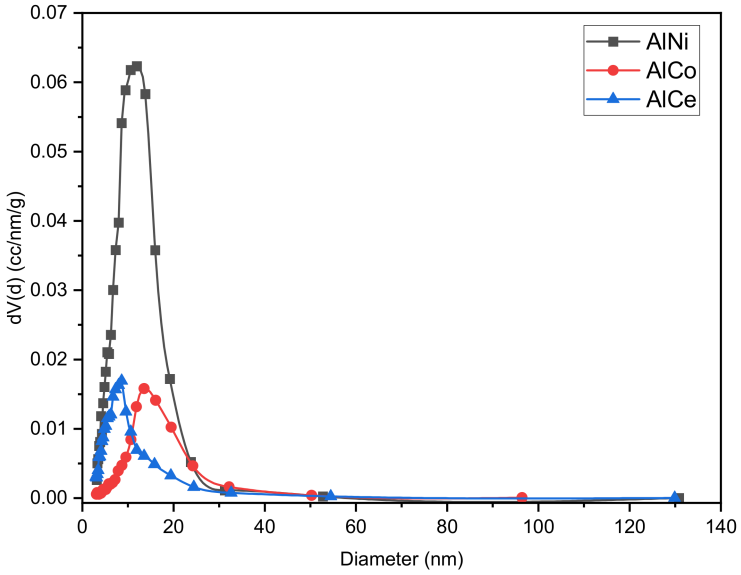


Figure 5. BJH pore size distribution of AlNi, AlCo, and AlCe catalysts derived from the N_2 desorption branch.

The quantitative textural parameters derived from the adsorption isotherms are reported in Table 2. The AlNi catalyst exhibits, as expected, the highest BET specific surface area (255.73 $m^2 \cdot g^{-1}$) and total pore volume (0.708 $cm^3 \cdot g^{-1}$), confirming the highly developed porous structure inferred from its isotherm. AlCe shows a significantly lower surface area (56.76 $m^2 \cdot g^{-1}$) and pore volume (0.174 $cm^3 \cdot g^{-1}$), while AlCo presents an intermediate surface area and pore volume (73.675 $m^2 \cdot g^{-1}$, 0.224 $cm^3 \cdot g^{-1}$). The mean pore diameters calculated by the BJH method (11.94 nm for AlNi, 13.55 nm for AlCo, and 8.64 nm for AlCe) lie entirely within the mesoporous range (2–50 nm), further corroborating the type IV classification.

Table 2. Textural properties of AlNi, AlCo, and AlCe catalysts determined by N_2 physisorption.

Catalyst	S_{BET} (m^2/g)	V_{pore} (cm^3/g)	Diam. DV(d) (nm)
AlNi	255.73	0.708	11.94
AlCo	73.675	0.224	13.55
AlCe	56.76	0.174	8.64

Overall, the combined analysis of isotherm shape, hysteresis loop type, and BJH pore size distribution confirms that all catalysts are predominantly mesoporous, with AlNi showing the most developed and interconnected pore network.

2.1.4. SEM–EDX Characterization

Representative SEM micrographs recorded at different magnifications reveal that all catalysts consist of irregularly shaped particles forming agglomerated structures, which is characteristic of oxide materials synthesized by co-precipitation methods. Although overall similar, SEM gives evidence of some important differences. As shown in Figure 6, the AlNi catalyst exhibits a highly fragmented and loosely packed morphology composed of relatively small primary particles, assembled into larger agglomerates. The presence of numerous interparticle voids and open spaces is clearly observed, particularly at lower magnifications. This morphology is fully consistent with the high BET specific surface area (255.73 $m^2 \cdot g^{-1}$) and large total pore volume (0.708 $cm^3 \cdot g^{-1}$) determined from N_2 physisorption, indicating a well-developed mesoporous network dominated by accessible

interparticle porosity. In contrast the AlCo catalyst displays more compact agglomerates with larger and denser particles. This observation correlates well with the lower surface area (73.675 $m^2 \cdot g^{-1}$) and pore volume (0.224 $cm^3 \cdot g^{-1}$) obtained from nitrogen adsorption–desorption measurements, suggesting a less open mesoporous structure and a higher degree of particle packing. On the other hand, the AlCe catalyst shows a comparatively heterogeneous morphology characterized by irregular agglomerates and locally dense regions. The particles appear more strongly sintered, consistent with the lowest pore volume (0.174 $cm^3 \cdot g^{-1}$) and smaller average pore diameter (8.64 nm) derived from BJH analysis.

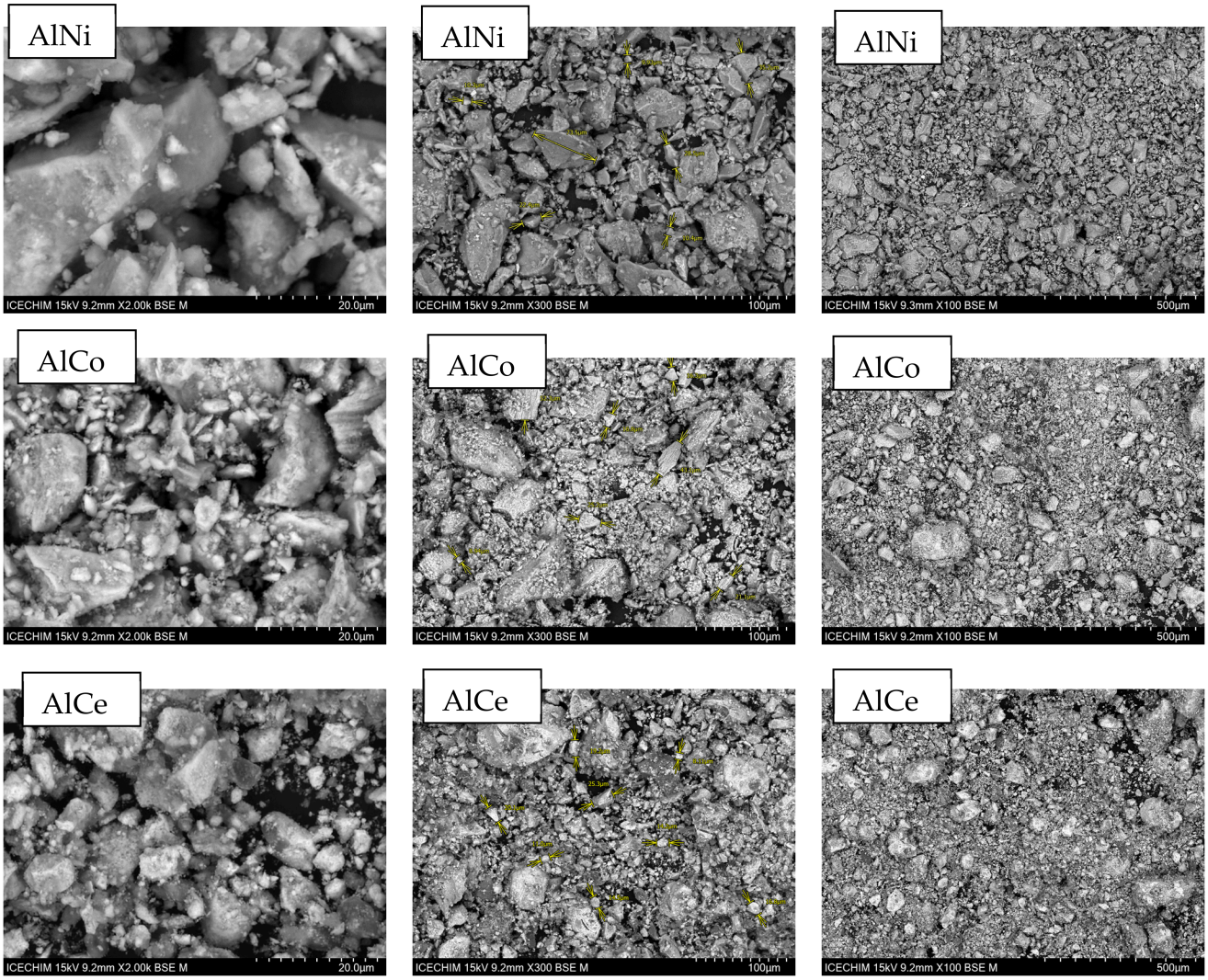


Figure 6. SEM micrographs of AlNi, AlCo, and AlCe catalysts recorded at different magnifications.

The SEM observations provide strong morphological evidence supporting the conclusions drawn from the nitrogen adsorption–desorption isotherms. The progressive decrease in surface area and pore volume from AlNi to AlCo and AlCe directly mirrors the transition from highly open, loosely aggregated structures to more compact particle assemblies, explaining the differences observed in the shape, and the extent of the hysteresis loops (H2(b) for AlNi, H2(b)→H3 tendency for AlCo and AlCe).

EDX spectra (Figure 7) collected from all samples confirm the presence of aluminum and the corresponding second metal (Ni, Co, or Ce), with no detectable impurities within the detection limits of the technique. The elemental signals are uniformly distributed across the analyzed regions, indicating successful incorporation of the metal species into the mixed-oxide matrix during the co-precipitation process. This compositional homogeneity

supports the reliability of the textural and catalytic comparisons among the three materials, as the observed differences in porosity and morphology arise primarily from structural effects rather than compositional inhomogeneity.

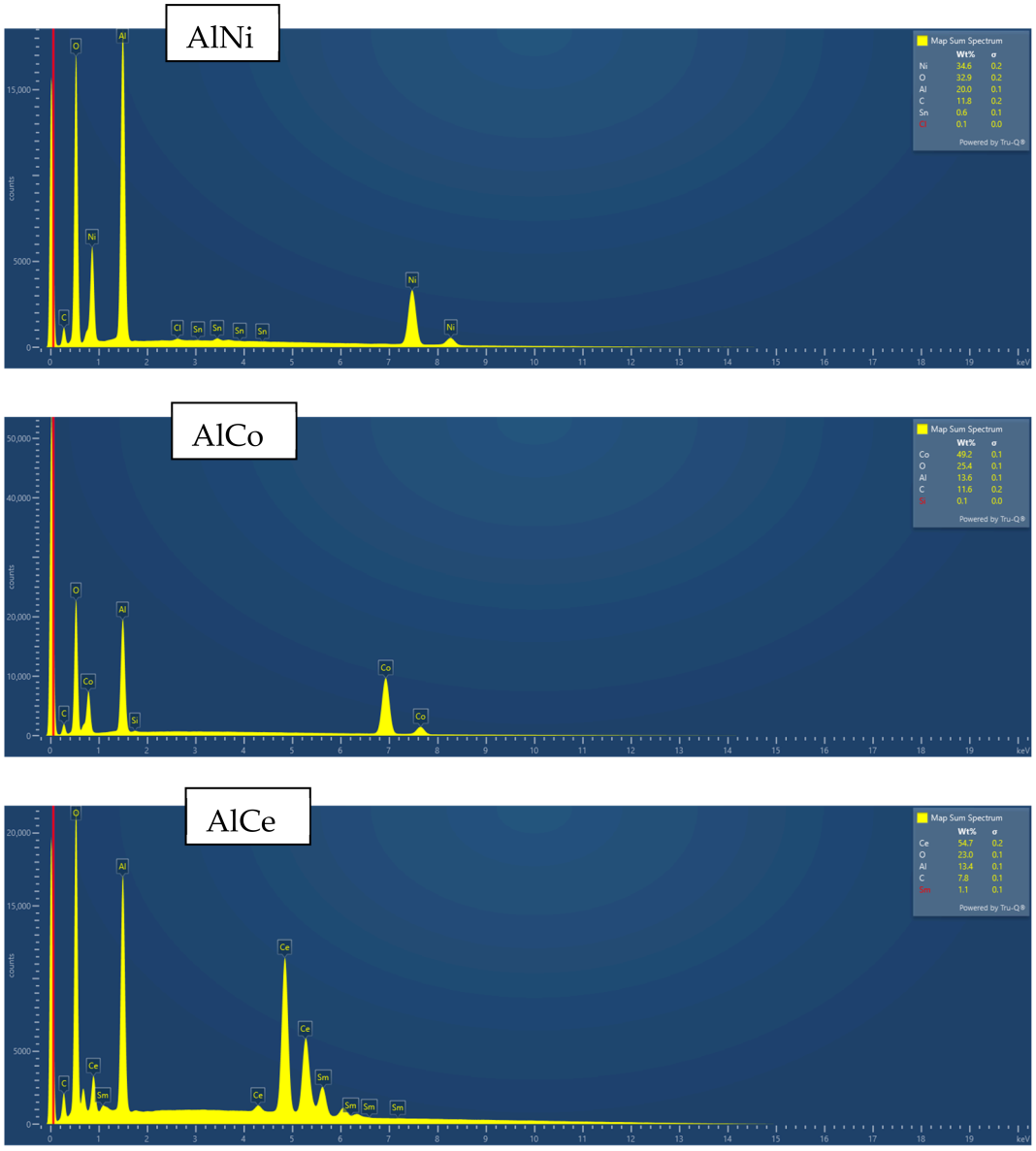


Figure 7. Representative EDX spectra of AlNi, AlCo, and AlCe catalysts.

Overall, SEM–EDX and N_2 physisorption results reveal a clear structure–texture relationship, with particle aggregation and interparticle voids playing a key role in determining surface accessibility and mesoporosity. In this context, AlNi shows the most advantageous morphology for catalytic applications demanding high accessible surface area.

2.1.5. TGA–DTG Analysis

The TGA–DTG profiles presented in Figures 8 and 9 exhibit a multistep mass-loss behavior for all catalysts, characterized by dominant low- and intermediate-temperature events and subsequent thermal stabilization at higher temperatures. While analyzing these results, we should note that, before the TGA-DTG experiment, the samples were calcined at 600 °C for 4 h under static air atmosphere, therefore the surface was already reconstructed and cleaned. Thus, most of the surface species prior to the TGA-DTG experiments were coming from moisture accumulated at the surface during exposure to ambient between

calcination and the thermogravimetric analysis. The clean surface after calcination likely contains predominantly Lewis acid centers and some isolated Brønsted centers. Upon exposure to moisture, the Lewis acid centers turn into Brønsted acid sites by dissociative water adsorption. Water on Lewis acid sites, consisting of coordinatively unsaturated metal cations, is likely less strongly bound than water dissociated at Brønsted acid sites and is therefore desorbed at lower temperatures, in our case in the 140–275 °C range, whereas true Brønsted sites desorb water at temperatures above 275 °C.

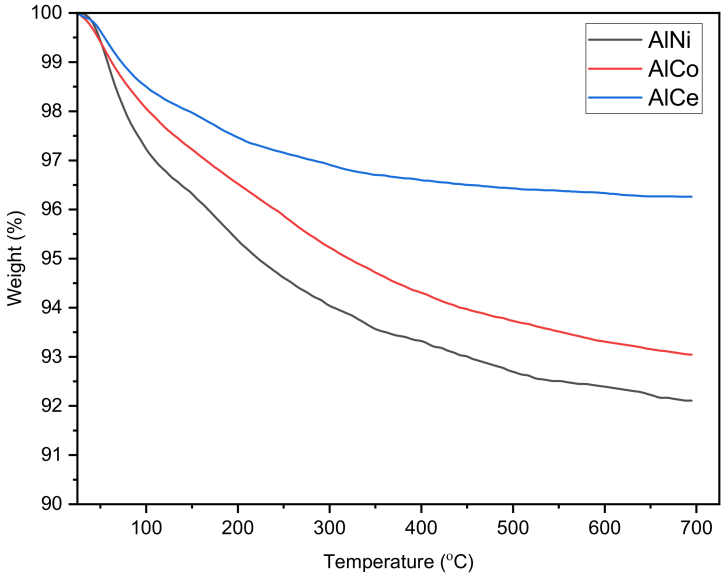


Figure 8. Thermogravimetric (TGA) weight-loss profiles of AlNi, AlCo, and AlCe catalysts.

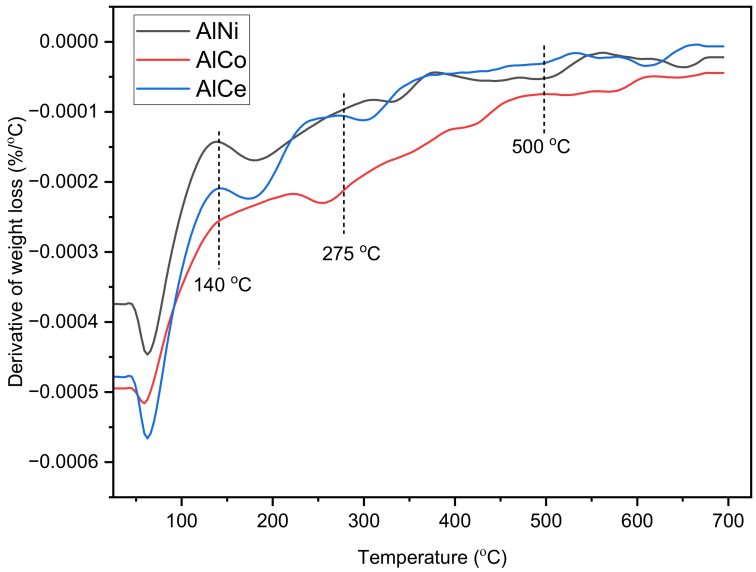


Figure 9. Derivative thermogravimetric (DTG) curves of AlNi, AlCo, and AlCe catalysts.

Along these lines, in the low-temperature range, up to approximately 140 °C, a noticeable weight decrease is observed for all catalysts, which is attributed primarily to the desorption of physically adsorbed moisture and weakly bound volatile species accumulated on the catalyst surface during the period between catalyst calcination and thermal analysis. The weight loss follows the order AlNi (3.55%) > AlCo (2.64%) > AlCe (1.87%), consistent with the DTG minima centered below ~140 °C. This trend correlates directly with the textural properties obtained from N_2 physisorption: AlNi exhibits the highest BET surface

area (255.73 $m^2 \cdot g^{-1}$) and pore volume (0.708 $cm^3 \cdot g^{-1}$), providing a larger accessible surface for moisture adsorption, whereas AlCe shows the lowest pore volume (0.174 $cm^3 \cdot g^{-1}$) and a less developed porous network, resulting in lower moisture uptake.

With increasing temperature, a second mass-loss step is evident between ~140 and 275 °C, with values of 2.17% (AlNi), 1.88% (AlCo), and 1.11% (AlCe). In this temperature region desorption of strongly H-bonded physisorbed water clustering at acid sites usually occurs, from condensation of vicinal surface OH groups, most likely on Lewis acid sites. This interval is also commonly associated with the removal of more strongly retained water within mesopores/interparticle voids, along with partial elimination of labile associated surface hydroxyl species [81]. The lower magnitude for AlCe again reflects its reduced surface accessibility and more compact morphology.

At higher temperatures, beyond 275 °C and approaching 500 °C, the mass loss is likely associated with dehydroxylation of isolated Al–OH constituting strong Brønsted acid sites. Therefore, this region of the derivative of the thermogravimetric analysis may be used, with caution, as a rough estimate of the concentration and strength of the Brønsted acid sites present on the samples.

Based on our results, the peaks shown in Figure 9 at ~400 °C for AlCo, and those at ~310 °C and ~350 °C for AlCe and AlNi, respectively, suggest at least two distinct Brønsted acid site populations coexisting on each surface, a well-established finding for alumina-based mixed oxides. We speculate these species correspond to isolated Al–OH or Al–OH–Co^{3+} bridges with high polarization, and bridging M–OH–Al with low polarization—where M is either Ce^{3+} or Ni^{2+}, respectively. This interpretation is consistent with stronger acid strength of the acid sites on AlCo compared to the other two samples suggested by the XPS results.

In this region, the catalysts exhibit additional gradual mass losses of 1.58% (AlNi), 1.76% (AlCo), and 0.60% (AlCe), accompanied by broader DTG features. In calcined oxide catalysts, this region is typically linked to progressive dehydroxylation (condensation of surface –OH groups) [82]. The relatively larger loss for AlNi and AlCo suggests a higher concentration of surface hydroxyls and/or a greater number of accessible adsorption sites, which is consistent with their larger specific surface area and more open microstructures compared with AlCe.

Above approximately 500 °C, the mass becomes nearly constant, indicating good thermal stability of the oxide frameworks. Only minor additional weight losses are recorded: 0.57% (AlNi), 0.68% (AlCo), and 0.16% (AlCe). The very small changes in this temperature range confirm that, after calcination, the catalysts contain limited amounts of thermally labile species and that the active oxide phases are stable up to 700 °C under inert conditions.

Overall, the total weight losses across the entire temperature range are approximately 7.87% (AlNi), 6.96% (AlCo), and 3.74% (AlCe), highlighting a clear trend: catalysts with higher surface area and pore volume undergo larger mass losses due to a greater capacity to adsorb and retain water and surface species. Overall, the TGA–DTG results strongly support the conclusions drawn from BET and SEM analyses: AlNi, characterized by the highest surface area and the most open/agglomerated morphology, shows the greatest moisture/surface-species uptake, whereas AlCe, with lower porosity and more compact domains, exhibits the lowest mass loss and the highest apparent thermal inertness.

2.1.6. FTIR-Py Analysis of Surface Acidity

The acidic properties of the AlNi, AlCo, and AlCe catalysts were investigated by Fourier transform infrared spectroscopy of adsorbed pyridine (FTIR-Py). The experimental steps applied in this study were adopted from our previous work [83] and applied identically to all samples in order to ensure a consistent and reliable comparison.

Representative FTIR-Py spectra of the catalysts are shown in Figure 10. Three characteristic absorption bands are clearly observed at approximately 1540, 1480, and 1437 cm^{-1} [84,85]. The band centered at ~1540 cm^{-1} is attributed to pyridinium ions formed upon protonation of pyridine, indicating the presence of Brønsted acid sites. The absorption at ~1437 cm^{-1} corresponds to pyridine coordinatively bonded to Lewis acid sites, while the band at ~1480 cm^{-1} arises from overlapping vibrations of pyridine interacting simultaneously with both Brønsted and Lewis acid sites. These band assignments are consistent with well-established interpretations reported in the literature [84,86–88].

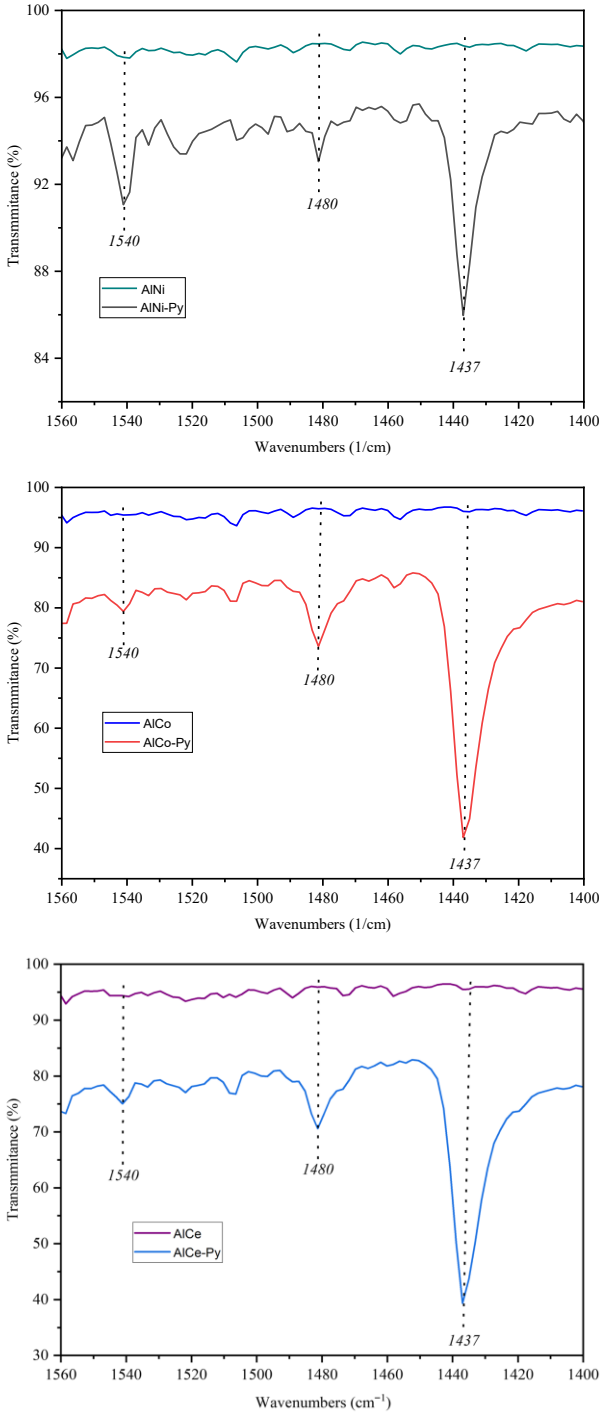


Figure 10. FTIR-Py spectra of AlNi, AlCo, and AlCe catalysts showing characteristic bands of Lewis and Brønsted acid sites.

Quantitative determination of the surface acidity was performed using the method proposed by Emeis [89], based on the integrated areas of the characteristic absorption bands and their respective molar extinction coefficients. The concentrations of Brønsted (C_B) and Lewis (C_L) acid sites were calculated using Equations (1) and (2), taking into account the pellet geometry and sample mass. The resulting acidity values are summarized in Table 3.

$$C_B = \frac{\pi}{IMEC_B} \cdot \frac{r^2}{w} \cdot A_{1540} \quad (1)$$

$$C_L = \frac{\pi}{IMEC_L} \cdot \frac{r^2}{w} \cdot A_{1437} \quad (2)$$

where C_L and C_B (μmol/g) are the concentrations of Lewis and Brønsted acid sites; A_{1437} and A_{1540} are the integrated areas of the bands at 1437 and 1540 cm^{-1}; and $IMEC_L$ and $IMEC_B$ are the integration molar extinction coefficients, 2.22 and 1.67 cm/μmol, respectively. r (cm) is the wafer radius, and w (g) is the wafer weight.

Table 3. Concentrations of Lewis and Brønsted acid sites of AlNi, AlCo, and AlCe catalysts determined by FTIR-Py.

Catalyst	Lewis Conc. (C_L) mmol/g	Brønsted Conc. (C_B) mmol/g	Total Conc. mmol/g	C_L/C_B
AlNi	7.061	2.144	9.205	3.30
AlCo	6.178	0.366	6.544	16.88
AlCe	4.184	0.282	4.466	14.84

The results reveal that all catalysts are predominantly characterized by Lewis acidity, as indicated by significantly higher C_L values compared to C_B. Among the investigated materials, AlNi exhibits the highest total acidity (9.205 mmol g^{-1}), with a more equilibrated contribution from both Lewis (7.061 mmol g^{-1}) and Brønsted (2.144 mmol g^{-1}) acid sites, resulting in the lowest C_L/C_B ratio (3.30). This behavior suggests a more balanced distribution of acid sites on the AlNi surface. In contrast, AlCo and AlCe display much higher C_L/C_B ratios (16.88 and 14.84, respectively), reflecting a strong predominance of Lewis acid sites and a limited contribution of Brønsted acidity.

These acidity trends correlate well with the textural and morphological properties discussed previously. The higher surface area and pore volume of AlNi, together with its more open and fragmented morphology, favor the formation and accessibility of both Lewis and Brønsted acid sites. Conversely, the lower porosity and more compact particle assemblies of AlCo and AlCe restrict the accessibility of Brønsted sites, leading to surfaces dominated by Lewis acidity. Overall, the FTIR-Py results demonstrate that the nature and distribution of acid sites are governed by a combined effect of chemical composition and the structural and textural characteristics of the catalysts. XRD analysis confirms that each catalyst contains distinct oxide phases ($NiAl_2O_4$/NiO, $CoAl_2O_4$/Co_3O_4, and $CeAlO_3$/CeO_2), which generate different local chemical environments for acid site formation. These compositional differences, together with variations in crystallite size, surface area, and porosity, determine both the strength and accessibility of Lewis and Brønsted acid sites, ultimately influencing their catalytic performance in ammonia decomposition.

2.2. Catalytic Performance Evaluation

The catalytic performance of the AlNi, AlCo, and AlCe catalysts in ammonia decomposition was systematically evaluated as a function of reaction temperature and gas hourly space velocity (GHSV), as illustrated in Figures 11 and 12. The results clearly demonstrate that ammonia conversion is strongly governed by both reaction temperature and contact

time between the reactant stream and the catalyst surface, reflecting the intrinsic kinetics of ammonia decomposition and the structure and accessibility of active sites.

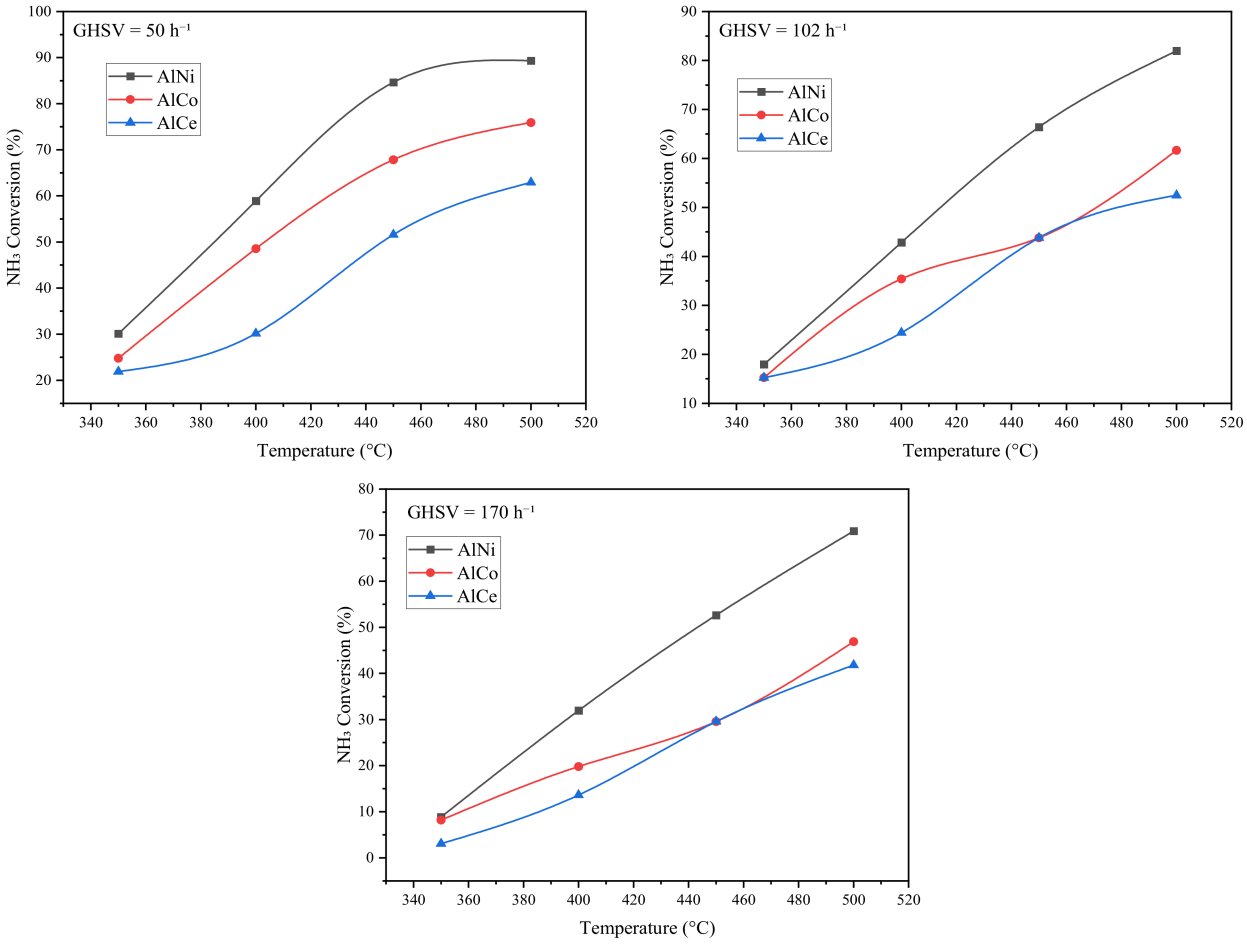


Figure 11. Effect of reaction temperature on ammonia conversion over AlNi, AlCo, and AlCe catalysts at different GHSV values (50, 102, and 170 h^{-1}).

As shown in Figure 11, ammonia conversion increases monotonically with increasing temperature over the investigated range of 350–500 °C for all catalysts. At a fixed GHSV of 50 h^{-1}, the highest conversions were achieved at 500 °C, reaching 89.34% for AlNi, 75.91% for AlCo, and 62.91% for AlCe. This trend confirms the endothermic nature of ammonia decomposition and the enhanced activation of surface reaction pathways at elevated temperatures. Across the entire temperature range, the catalytic activity follows the consistent order AlNi > AlCo > AlCe, indicating intrinsic differences in the catalytic efficiency of the three materials.

The superior performance of the AlNi catalyst can be directly correlated with its physicochemical properties. AlNi exhibits the highest BET specific surface area and pore volume, as well as a more uniform mesoporous structure, which promotes efficient diffusion of reactants and products. In addition, FTIR-Py analysis revealed that AlNi possesses the highest total acidity with the most balanced distribution of Lewis and Brønsted acid sites (lowest C_L/C_B ratio). Such a combination of high surface accessibility and favorable acid site distribution is expected to facilitate ammonia adsorption and subsequent N–H bond cleavage, thereby enhancing the overall reaction rate.

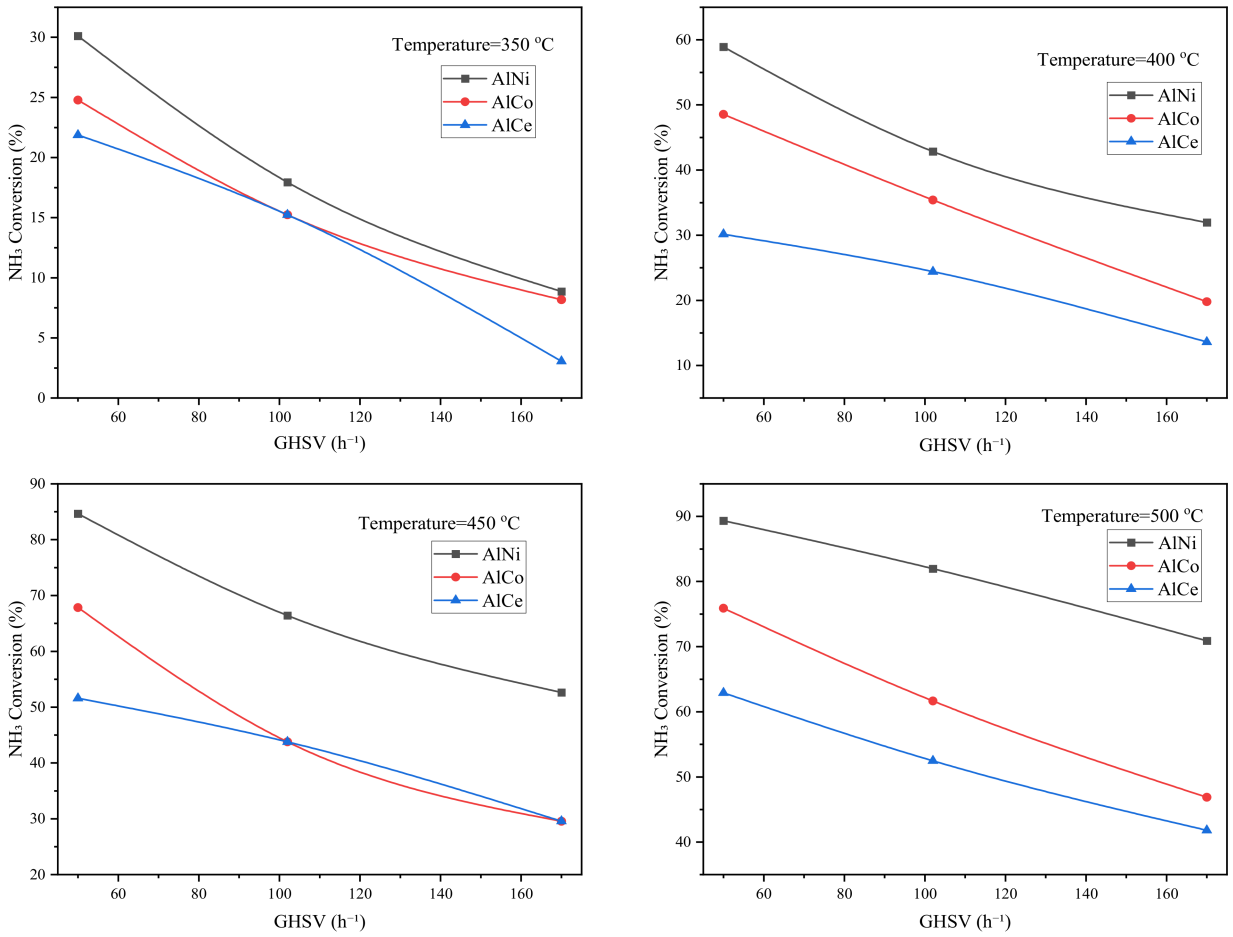


Figure 12. Effect of gas hourly space velocity (GHSV) on ammonia conversion over AlNi, AlCo, and AlCe catalysts at different reaction temperatures (350–500 °C).

On the other hand, the XPS data are a good predictor of the Lewis acid character of the surface of these materials. The O 1s and Al 2p binding energy data provide direct electronic fingerprints of the surface electrophilicity, which governs the acid strength of the mixed-oxide surface. The higher the O 1s binding energy, the stronger the withdrawn oxygen electron density, resulting in more electrophilic metal centers and thus stronger Lewis acid centers. Also, the higher Al 2p binding energy translates into more electron-deficient Al^{3+} ions and thus stronger Lewis acid character at aluminum sites. Along these lines, the Lewis acid strength in our mixed-oxide catalyst should vary in the order AlCo > AlNi > AlCe. However, while correlating the XPS results with the performance of our catalysts, we should also factor in the more than three-fold higher specific surface area of the AlNi catalyst compared to the AlCo one, which compensates for its weaker acid strength through density of sites.

Figure 12 illustrates the effect of GHSV on ammonia conversion at fixed temperatures of 350, 400, 450, and 500 °C. For all catalysts, increasing GHSV from 50 to 170 h^{-1} leads to a pronounced decrease in ammonia conversion, highlighting the critical role of residence time in this reaction. At 350 °C, ammonia conversion over AlNi decreases from 30.11% at GHSV = 50 h^{-1} to 8.86% at GHSV = 170 h^{-1}. Similar trends are observed for AlCo and AlCe, although at lower absolute conversion levels, consistent with their lower specific surface area, thus decreased active site density of these samples.

Even at the highest reaction temperature of 500 °C, the effect of space velocity remains significant. For the AlNi catalyst, ammonia conversion decreases from 89.34% to 70.90% as GHSV increases from 50 to 170 h^{-1}, while corresponding decreases from 75.91% to 46.89%

and from 62.91% to 41.81% are observed for AlCo and AlCe, respectively. These results indicate that, despite enhanced reaction kinetics at elevated temperatures, insufficient contact time limits the extent of ammonia decomposition, particularly for catalysts with lower surface area and fewer accessible active sites.

The observed performance trends are fully consistent with the structural and textural characteristics of the catalysts. The higher sensitivity of AlCe to increasing GHSV can be attributed to its lower surface area, smaller pore size and volume, and more compact morphology, as revealed by nitrogen adsorption–desorption and SEM analyses. In contrast, the more open and loosely aggregated structure of AlNi, combined with its higher density of acid sites and thermal stability, allows it to better sustain catalytic activity even under shorter contact times.

Overall, these results demonstrate that efficient ammonia decomposition over Al-based catalysts requires a synergistic combination of high surface area, accessible mesoporosity, and an appropriate distribution of surface acid sites. Catalytic activity is enhanced by increasing the reaction temperature and decreasing GHSV, in agreement with kinetic considerations and previous reports in the literature [21,27,90]. Among the investigated materials, AlNi provides the most favorable balance between structural, textural, and chemical properties, resulting in superior catalytic performance over the entire range of operating conditions studied.

Beyond textural and morphological effects, the nature of surface acidity emerges as a decisive factor in governing ammonia decomposition. The catalytic results clearly demonstrate that surface acidity, particularly Lewis acid sites, plays a critical role in the activation of NH_3 molecules. Ammonia is a strongly basic molecule, and its initial adsorption and activation preferentially occur on electron-deficient Lewis acid sites, which facilitate coordination of the nitrogen lone pair and promote subsequent stepwise N–H bond scission. Consequently, catalysts exhibiting a higher concentration of accessible Lewis acid sites enable larger amounts of NH_3 adsorption and thus more efficient surface activation, leading to increased conversion levels.

In this context, the superior performance of the AlNi catalyst can be directly attributed to its highest total acidity and more balanced Lewis-to-Brønsted acid site ratio, as revealed by FTIR-Py analysis, despite its slightly weaker Lewis acid centers compared to AlCo. The abundance of Lewis acid sites, combined with high surface accessibility, increases the density of effective NH_3 adsorption sites and accelerates the rate-determining N–H bond cleavage steps. This interpretation is fully consistent with previous studies, which have shown that ammonia decomposition is favored on catalysts with high Lewis acidity, whereas Brønsted acid sites mainly contribute to weaker and less reactive adsorption modes [25,91,92]. Accordingly, the strong correlation observed in this work between ammonia conversion and Lewis acidity provides compelling evidence that surface acid properties constitute a primary controlling factor in ammonia decomposition over mixed oxide-based catalysts.

2.3. Kinetic Modeling of Ammonia Decomposition

The experimental data described in previous paragraphs were used to develop a kinetic model for ammonia decomposition, for each of the catalysts considered in our study. The mechanism accepted in the literature for this process is a Langmuir–Hinshelwood one, postulating that the reaction takes place between adsorbed species. Recent studies, such as the one published by Guo and Vlachos [93], used DFT analyses to support the stepwise mechanism based on the elementary steps, starting with ammonia adsorption on active

centers X (3), followed by stepwise dehydrogenation, steps (4) to (6), and then desorption of reaction products:

$$NH_{3(g)} + X \rightleftarrows NH_3X \quad (3)$$

$$NH_3X + X \rightleftarrows NH_2X + HX \quad (4)$$

$$NH_2X + X \rightleftarrows NHX + HX \quad (5)$$

$$NHX + X \rightleftarrows NX + HX \quad (6)$$

$$2NX \rightleftarrows N_2 + 2X \quad (7)$$

$$2HX \rightleftarrows H_2 + 2X \quad (8)$$

In these steps, X represents the catalyst active centers and JX represents the adsorbed species (J—NH_3, NH_2, NH, H, N). The rate-determining step (RDS) depends on the specific metal and it is heavily debated in the literature.

Simonsen et al. [94] and Mizoguchi et al. [95] showed that the ammonia decomposition follows a volcano plot relationship based on metal–nitrogen binding energy. If Ru is a metal sitting at the apex of the volcano, metals to its left (i.e., iron) bind nitrogen too strongly, consequently making recombinative desorption the rate-determining step, whereas the metals to its right (i.e., Ni, Co) bind nitrogen weakly, making the initial activation of ammonia difficult. The classical kinetic model for ammonia synthesis (and, by reciprocity, its decomposition), initially developed by Temkin and Pyzhev, assumes that nitrogen adsorption/desorption is the RDS [96]. In our study, based on aspects presented and the fact that the catalyst contains Ni and Co, and also considering results reported in other published studies [97–100], step (4) was considered the limiting step.

The rate expression derived based on this assumption is given by Equation (9):

$$r = \frac{k \cdot K_{NH_3}^2 \cdot p_{NH_3}^2}{\left(K_{NH_3} \cdot p_{NH_3} + \frac{p_{H_2}^{3/2}}{K_{H_2}^{3/2}} + \left(1 + \sqrt{\frac{p_{H_2}}{K_{H_2}}}\right)\right)^2} \quad (9)$$

where k is the rate expression and K_J represents the adsorption equilibrium constants for ammonia and hydrogen, respectively.

Both rate constants and adsorption equilibrium constants can be expressed by their Arrhenius forms as follows:

$$k = k_0 \cdot \exp\left(-\frac{E}{R_G \cdot T}\right);\ K_J = K_{J0} \cdot \exp\left(-\frac{\Delta H_{ads,J}}{R_G \cdot T}\right),\ J = NH_3,\ H_2 \quad (10)$$

The rate Equation (9) contains six kinetic parameters (three frequency factors and three activation energies or adsorption enthalpies) and their values were estimated by an integral method using measured ammonia conversions. To determine the conversion values required in the least-square approach, a pseudo-homogeneous model of the chemical reactor assuming plug-flow of the gas phase was implemented. These assumptions correspond to the ammonia mass balance equation:

$$\frac{dx_A}{dz} = \frac{S_T}{F_{MA,0}} \cdot \rho_b \cdot r_A;\ z = 0,\ x_A = 0 \quad (11)$$

The estimation of kinetic parameters was carried out by the MATLAB® 2025b programming environment using the "lsqcurvefit" function and the adequacy of the model was assessed based on both the correlation coefficient (R^2) and statistically evaluated confidence

intervals. The resulting kinetic parameter values, along with their 95% confidence intervals, are given in Table 4.

Table 4. Estimated kinetic parameters and their 95% confidence intervals.

Parameter	Unit	Catalyst		
		AlNi	**AlCo**	**AlCe**
k_0	$\frac{kmol}{s \cdot kg_{cat}}$	99.213 (1 ± 0.182)	1.163 (1 ± 0.032)	1.121 (1 ± 0.065)
E	$\frac{J}{mol}$	7.097×10^4 (1 ± 0.011)	5.692×10^4 (1 ± 0.003)	5.845×10^4 (1 ± 0.007)
$K_{NH_3,0}$	atm^{-1}	0.123 (1 ± 0.057)	0.168 (1 ± 0.038)	0.177 (1 ± 0.162)
$\Delta H^{ads}_{NH_3}$	$\frac{J}{mol}$	-3.146×10^4 (1 ± 0.049)	-2.988×10^4 (1 ± 0.011)	-2.992×10^4 (1 ± 0.045)
$K_{H_2,0}$	atm	8.461×10^{-2} (1 ± 0.164)	6.038×10^{-2} (1 ± 0.042)	4.840×10^{-2} (1 ± 0.208)
$\Delta H^{ads}_{H_2}$	$\frac{J}{mol}$	-6.663×10^3 (1 ± 0.069)	-8.117×10^3 (1 ± 0.043)	-8.055×10^3 (1 ± 0.205)
R^2	-	0.986	0.991	0.933

Although the AlNi catalyst exhibits a slightly higher apparent activation energy, its significantly larger pre-exponential factor (k_0) results in the highest overall reaction rate. The apparent activation energies obtained in this work (56.92–70.97 kJ mol^{-1}) are within the lower range of values reported in the literature for ammonia decomposition over transition-metal-based catalysts. For example, Ni/Al_2O_3 monolith catalysts exhibit an activation energy of approximately 113.4 kJ mol^{-1} [101], while bimetallic systems such as 5Ni-1Ru/CeO_2 and 2.5Ni0.5Ru/CeO_2 show values of 124 and 107 kJ mol^{-1}, respectively [98]. Even higher activation barriers have been reported for Ru/SiO_2 catalysts (~301 kJ mol^{-1}) [102], whereas Ru/Al_2O_3 catalysts typically present activation energies around 71.3 kJ mol^{-1} [103]. Other oxide-supported systems, such as Ru/Al_2O_3 and Ru/K–CaO catalysts, exhibit activation energies in the range of 75–105 kJ mol^{-1} [104,105].

Compared with these reported values, the catalysts developed in this work display relatively moderate activation energies, particularly for AlCo and AlCe (56.92 and 58.45 kJ mol^{-1}), indicating that the mixed Al–M oxide structure provides favorable active environments for ammonia activation. In addition, the superior catalytic performance of AlNi, despite its slightly higher activation energy, suggests that the overall reaction rate is governed not only by the activation barrier, but also by the frequency of effective surface reactions, as reflected by the significantly larger pre-exponential factor.

In order to validate the estimated kinetic parameters, several sets of experimental data were used to verify model predictions. The results, presented in the parity diagrams in Figure 13, together with the R^2 values and 95% confidence intervals in Table 4, show good adequacy of the kinetic model.

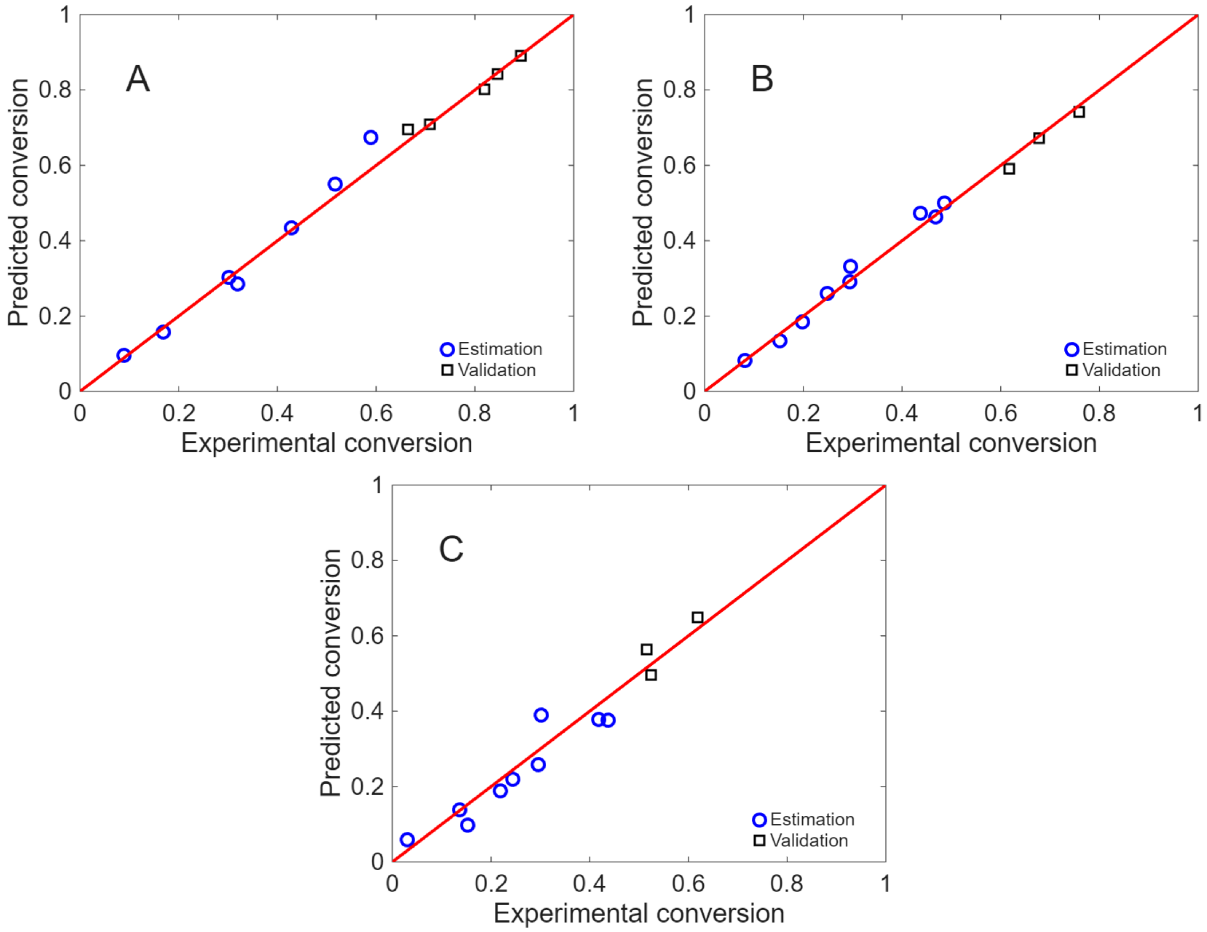


Figure 13. Parity diagrams for AlNi (**A**), AlCo (**B**) and AlCe (**C**) catalysts.

3. Material and Methods

3.1. Materials

All chemicals used in the present study were of analytical grade. Aluminum nitrate nonahydrate ($Al(NO_3)_3 \cdot 9H_2O$, purity $\geq$ 98%) and ammonium hydroxide solution (NH_4OH, 35 wt%) were supplied by Chimreactiv (Bucharest, Romania). Nickel nitrate hexahydrate ($Ni(NO_3)_2 \cdot 6H_2O$, purity $\geq$ 99%) was purchased from Acros Organics (Waltham, MA, USA). Cobalt(II) acetate tetrahydrate ($Co(CH_3COO)_2 \cdot 4H_2O$, purity $\geq$ 99.9%) and cerium nitrate hexahydrate ($Ce(NO_3)_3 \cdot 6H_2O$, purity $\geq$ 99.9%) were obtained from Merck (Darmstadt, Germany).

3.2. Catalysts Synthesis

Aluminum-based mixed-oxide catalysts (AlNi, AlCo, and AlCe) were synthesized using the co-precipitation method [47,86] with metal precursor salts in order to achieve a nominal atomic ratio of aluminum to the second metal (Ni, Co, or Ce) of 1:1. Specifically, a mixture consisting of 16.9 g of $Al(NO_3)_3 \cdot 9H_2O$ and 11.2 g of $Co(CH_3COO)_2 \cdot 4H_2O$ was used for the preparation of the aluminum–cobalt-based catalyst, denoted as AlCo. For the aluminum–nickel-based catalyst (AlNi), 16.9 g of $Al(NO_3)_3 \cdot 9H_2O$ and 13.1 g of $Ni(NO_3)_2 \cdot 6H_2O$ were employed. In the case of the aluminum–cerium-based catalyst (AlCe), 16.9 g of $Al(NO_3)_3 \cdot 9H_2O$ and 19.5 g of $Ce(NO_3)_3 \cdot 6H_2O$ were used.

For each catalyst, the corresponding precursor mixture was dissolved in 1000 mL of distilled water, and the resulting solution was heated to 60 °C under continuous magnetic stirring at 1500 rpm for 30 min. Throughout the entire synthesis process, a constant flow of nitrogen gas was passed through the solution to maintain an inert atmosphere.

The precipitation reaction was carried out at 60 °C under basic conditions (pH 10–11) using a 35 wt% aqueous ammonia solution. Ammonium hydroxide was added dropwise, and the reaction was allowed to proceed for 60 min. Since pH control is critical at this stage for nucleation and phase selectivity, the pH value was monitored during the precipitation step using a calibrated pH meter and pH indicator paper. After 60 min, the resulting precipitate was separated by decantation and washed with distilled water to remove residual reaction by-products, particularly the formed salts. The obtained solids were then dried at 200 °C for 6 h. Subsequently, the dried materials were calcined at 600 °C for 4 h in a static ambient atmosphere, leading to the formation of the active metal oxide catalytic phases corresponding to AlCo, AlNi, and AlCe, respectively.

3.3. Catalysts Characterization Equipment

The catalysts were extensively examined by combining several complementary characterization methods, including X-ray diffraction (XRD) and photoelectron spectroscopy (XPS), scanning electron microscopy (SEM), thermogravimetric analysis coupled with differential thermogravimetry (TGA–DTG), textural analysis based on nitrogen adsorption–desorption, Fourier transform infrared (FTIR) spectroscopy, and surface acidity assessment via pyridine adsorption followed by FTIR analysis (FTIR-Py).

Crystalline phase identification was carried out by X-ray diffraction using a SmartLab diffractometer manufactured by Rigaku Corporation (Akishima, Japan), operated with Cu Kα radiation (λ = 0.15406 nm). The X-ray generator was set to an accelerating voltage of 45 kV and a tube current of 200 mA. Diffraction patterns were collected in parallel-beam mode within a 2θ angular range of 3–80°, employing a scanning speed of 6 °/min [47,48,83].

The surface chemistry was studied by X-ray photoelectron spectroscopy (XPS) using a K-Alpha instrument from Thermo Scientific (Thermo Fisher Scientific, Waltham, MA, USA) with a monochromatic Al Kα source (1486.6 eV) at a bass pressure of 2×10^{-9} mbar. Charging effects were compensated by a flood gun and binding energies were calibrated by placing the C 1s peak at 284.4 eV as the internal standard. A pass energy of 200 eV and 20 eV was used for survey and high-resolution spectra acquisition, respectively [47,48].

The surface morphology and microstructural features of the samples were investigated using a scanning electron microscope supplied by FEI Company (Hillsboro, OR, USA). Thermal stability and decomposition behavior were evaluated through TGA–DTG measurements performed on a thermal analysis system from METTLER TOLEDO (Zurich, Switzerland) [47,83]. These analyses were conducted between 25 and 700 °C under nitrogen atmosphere with a flow rate of 30 mL/min, applying a constant heating rate of 10 °C/min.

Textural characteristics, including surface area and pore structure, were determined by nitrogen physisorption measurements using a NOVA 2200e gas sorption analyzer from Quantachrome (Graz, Austria) [47,48,83]. Adsorption–desorption isotherms were acquired at 77.35 K over a relative pressure (p/p_0) interval from 0.005 to 1.0, and the resulting data were processed using NovaWin software (version 11.03). The specific surface area was calculated according to the Brunauer–Emmett–Teller (BET) approach, while the total pore volume and pore size distribution were estimated using the Barrett–Joyner–Halenda (BJH) method based on the desorption branch [47,48,83].

FTIR spectroscopy of adsorbed pyridine (FTIR-Py) was employed to determine the concentrations of the acid sites of the catalysts. Measurements were carried out using an IRAffinity-1S spectrometer (Shimadzu, Kyoto, Japan) equipped with a GladiATR-10 accessory for attenuated total reflectance (ATR) [83,106]. The spectra were recorded in the wavenumber range of 1400–1560 cm^{-1} with a spectral resolution of 4 cm^{-1}. Pyridine adsorption was carried out by exposing 0.5 g of each catalyst to pyridine for 6 h at room temperature in a sealed capsule. Subsequently, the samples were thermally treated at

115 °C for 2 h to remove weakly physisorbed pyridine prior to FTIR analysis. Different sample amounts were used for the FTIR measurements as required by the practical aspects related to pellet preparation. The concentration of acid sites was calculated using the Emeis method, as described above, by normalizing the integrated peak area with respect to the sample mass—the wafer radius (*r*)—which was constant at 1.2 mm, and the corresponding molar extinction coefficients.

3.4. Catalytic Evaluation Studies

The catalytic studies were carried out in a vertical carbon steel tubular fixed-bed reactor (i.d. = 1.2 cm, h = 60 cm) loaded with 2.5 g of catalyst. All experiments were performed under atmospheric pressure (1 bar) within a temperature range of 350–500 °C, using temperature intervals of 75 °C. The volumetric feed flow rate of ammonia was varied between 3 and 10 L/h, corresponding to weight hourly space velocities (WHSV) of 50, 102, and 170 h^{-1}.

Ammonia conversion was determined using a gas chromatograph equipped with a thermal conductivity detector (TCD) (Agilent 6890N, Santa Clara, CA, USA) and a CP-Sil 5 CB capillary column, with helium employed as the carrier gas. The gas chromatograph was equipped with a sampling valve incorporating a 0.5 mL sample loop, ensuring accurate and reproducible gas sampling. The NH_3 concentration in the gas mixture at the reactor outlet was continuously monitored following the catalytic decomposition reaction.

The applied temperature program consisted of an initial step at 50 °C maintained for 1 min, followed by heating at a rate of 10 °C·min^{-1} up to 150 °C, where the temperature was held constant for 5 min.

4. Conclusions

A series of Al-based mixed-oxide catalysts (AlNi, AlCo, and AlCe) was rationally engineered through a coprecipitation route and investigated for catalytic ammonia decomposition. Structural characterization by XRD revealed the formation of well-defined aluminate phases, including $NiAl_2O_4$, $CoAl_2O_4$, and $CeAlO_3$, while XPS analysis confirmed the corresponding surface chemical states of Ni^{2+}, and mixed Co^{2+}/Co^{3+} and Ce^{3+}/Ce^{4+} species. The strong agreement between bulk crystalline phases investigated by XRD and the near-surface chemical states characterized by XPS indicates a high structural consistency of the synthesized mixed-oxide systems. XPS indicated the acid character of the catalysts' surface decreases in the order AlCo > AlNi > AlCe, with the AlNi catalyst having the highest specific surface area and pore volume, and the most equilibrated Lewis to Brønsted ratio, as determined from FTIR pyridine adsorption experiments.

The evaluation of the catalytic performance of synthesized samples revealed a clear activity trend (AlNi > AlCo > AlCe), with AlNi exhibiting the highest ammonia conversion over the investigated temperature range. Although the acidity of AlCo was found to be greater than that of AlNi, the superior catalytic performance of AlNi is most likely associated with its three-fold higher specific surface area, and a more equilibrated Lewis/Brønsted acidity, leading to more favorable surface kinetics, since both Lewis and Brønsted acid sites are involved in the reaction. Our experimental results confirmed the reaction mechanism, where ammonia is activated on the Lewis acid sites of the catalysts, while subsequent N–H bond cleavage proceeds through neighboring Brønsted acid sites, with this former step being rate limiting. Although AlNi shows a slightly higher apparent activation energy (70.97 kJ mol^{-1})—consistent with its weaker Lewis acid strength—its significantly larger pre-exponential factor results in the highest intrinsic reaction rate among the studied catalysts. The estimated activation energies (56.92–70.97 kJ mol^{-1}) fall within the lower

range of values reported in the literature for ammonia decomposition catalysts, indicating efficient NH_3 activation pathways.

Overall, the study demonstrates that, when combined with XRD, XPS is a powerful tool for elucidating electronic structure, bonding, and lattice integration in mixed-oxide systems. The results emphasize how electronic effects, such as inductive interactions and covalency, and structural factors, such as ionic size mismatch and disorder, can jointly be used to tune the surface chemistry and catalytic relevance of such materials. The combined structural, surface, and kinetic analyses demonstrate that catalytic performance is strongly governed by the interplay between catalyst electronic structure and kinetic parameters. Among the investigated materials, the AlNi catalyst provides the most favorable balance of structural characteristics, surface acidity, and intrinsic activity, highlighting its potential as an efficient non-noble metal catalyst for hydrogen production via ammonia decomposition.

Author Contributions: Conceptualization, D.M.C., R.D.; methodology, D.M.C., R.D., M.L.; validation, D.M.C.; R.D.; I.B., R.G.; formal analysis, D.M.C., R.D., G.V., M.L.; investigation, R.D., A.M.P., A.V., S.G.M., G.V.; resources, R.D., I.B., R.G., M.L.; data curation, D.M.C., R.D., I.B.; writing—original draft preparation, D.M.C., R.D., I.B.; writing—review and editing, R.D., M.L.; visualization, D.M.C.; supervision D.M.C. and R.D.; Project administration, D.M.C. All authors have read and agreed to the published version of the manuscript.

Funding: G.V. acknowledges the support of the PN 23.06 Core Program—ChemNewDeal, within the National Plan for Research, Development and Innovation 2022–2027, developed with the support of the Ministry of Research, Innovation and Digitalization, Project No. PN 23.06.02.01, InteGral.

Data Availability Statement: The original contributions presented in this study are included in the article. Further inquiries can be directed to the corresponding authors.

Conflicts of Interest: The authors declare no conflicts of interest.

References

1. Christensen, C.H.; Johannessen, T.; Sørensen, R.Z.; Nørskov, J.K. Towards an ammonia-mediated hydrogen economy? *Catal. Today* **2006**, *111*, 140–144. [CrossRef]
2. Germscheidt, R.L.; Moreira, D.E.B.; Yoshimura, R.G.; Gasbarro, N.P.; Datti, E.; dos Santos, P.L.; Bonacin, J.A. Hydrogen Environmental Benefits Depend on the Way of Production: An Overview of the Main Processes Production and Challenges by 2050. *Adv. Energy Sustain. Res.* **2021**, *2*, 2100093. [CrossRef]
3. He, T.; Pachfule, P.; Wu, H.; Xu, Q.; Chen, P. Hydrogen carriers. *Nat. Rev. Mater.* **2016**, *1*, 16059. [CrossRef]
4. Ristig, S.; Poschmann, M.; Folke, J.; Gómez-Cápiro, O.; Chen, Z.; Sanchez-Bastardo, N.; Schlögl, R.; Heumann, S.; Ruland, H. Ammonia Decomposition in the Process Chain for a Renewable Hydrogen Supply. *Chem. Ing. Tech.* **2022**, *94*, 1413–1425. [CrossRef]
5. Bell, T.E.; Torrente-Murciano, L. H2 Production via Ammonia Decomposition Using Non-Noble Metal Catalysts: A Review. *Top. Catal.* **2016**, *59*, 1438–1457. [CrossRef]
6. Wu, J.; Yang, L.; Xiang, C.; Liang, J.; Yang, H.; Li, D.; Sun, Y.; Lv, L.; Zhu, N. Research on Catalysts for Online Ammonia Hydrogen Production in Marine Engines: Performance Evaluation and Reaction Kinetic Modeling. *Catalysts* **2025**, *15*, 488. [CrossRef]
7. Hu, Z.-P.; Weng, C.-C.; Chen, C.; Yuan, Z.-Y. Two-dimensional mica nanosheets supported Fe nanoparticles for NH_3 decomposition to hydrogen. *Mol. Catal.* **2018**, *448*, 162–170. [CrossRef]
8. Armenise, S.; Cazaña, F.; Monzón, A.; García-Bordejé, E. In situ generation of COx-free H_2 by catalytic ammonia decomposition over Ru-Al-monoliths. *Fuel* **2018**, *233*, 851–859. [CrossRef]
9. Obata, K.; Kishishita, K.; Okemoto, A.; Taniya, K.; Ichihashi, Y.; Nishiyama, S. Photocatalytic decomposition of NH_3 over TiO_2 catalysts doped with Fe. *Appl. Catal. B Environ.* **2014**, *160–161*, 200–203. [CrossRef]
10. Lucentini, I.; Serrano, I.; Soler, L.; Divins, N.J.; Llorca, J. Ammonia decomposition over 3D-printed CeO_2 structures loaded with Ni. *Appl. Catal. A Gen.* **2020**, *591*, 117382. [CrossRef]
11. Hund, S.; Gómez-Cápiro, O.; Dembélé, K.; Berendts, S.; Lunkenbein, T.; Ruland, H.; Heppke, E.M.; Lerch, M. Fe_3Mo_3N: Crystal Structure, High-Temperature Behavior, and Catalytic Activity for Ammonia Decomposition. *Z. Für Anorg. Und Allg. Chem.* **2023**, *649*, e202300152. [CrossRef]
12. Wolf, M.; Fischer, N.; Claeys, M. Formation of metal-support compounds in cobalt-based Fischer-Tropsch synthesis: A review. *Chem. Catal.* **2021**, *1*, 1014–1041. [CrossRef]

13. Weidenthaler, C.; Schmidt, W.; Leiting, S.; Ternieden, J.; Kostis, A.; Ulucan, T.H.; Budiyanto, E. In-situ Investigations of Co@Al_2O_3 Ammonia Decomposition Catalysts: The Interaction between Support and Catalyst. *ChemCatChem* **2022**, *14*, e202200688. [CrossRef]
14. Wang, W.; Fu, Y.; Wang, W.; Xiang, M.; Chen, G.; Su, Y.; Duan, J. Ammonia decomposition over La-doped Al_2O_3 supported Co catalyst. *Ceram. Int.* **2024**, *50*, 36604–36614. [CrossRef]
15. Bell, T.E.; Ménard, H.; González Carballo, J.M.; Tooze, R.; Torrente-Murciano, L. Hydrogen production from ammonia decomposition using Co/γ-Al_2O_3 catalysts—Insights into the effect of synthetic method. *Int. J. Hydrogen Energy* **2020**, *45*, 27210–27220. [CrossRef]
16. Winter, F.L.; Diehl, P.; Telaar, P.; Watermann, C.M.; Kaluza, S.; Muhler, M.; Apfel, U.-P.; Zeidler-Fandrich, B. Influence of the catalyst precursor for cobalt on activated carbon applied in ammonia decomposition. *Catal. Today* **2024**, *429*, 114502. [CrossRef]
17. Okura, K.; Okanishi, T.; Muroyama, H.; Matsui, T.; Eguchi, K. Ammonia Decomposition over Nickel Catalysts Supported on Rare-Earth Oxides for the On-Site Generation of Hydrogen. *ChemCatChem* **2016**, *8*, 2988–2995. [CrossRef]
18. Li, C.; Su, X.; Chen, J.; Tang, T.; Xue, J.; Rac, V.; Rakić, V.; Chen, Y.; Du, X. Catalytic Ammonia Decomposition for COx-Free Hydrogen Production over Fumed SiO_2-Supported Co–Ni Bimetallic Catalysts. *Energy Fuels* **2024**, *38*, 16873–16881. [CrossRef]
19. Gong, X.-C.; Peng, C.; Li, Z.; Zhang, D.; Wang, B.-H.; Yao, J.-J.; Guo, J.-K.; Chen, G.-H.; Yin, S.-F. Spin-State Engineering of Co-Based Catalysts Enables Efficient Ammonia Decomposition for Hydrogen Production. *Energy Fuels* **2025**, *39*, 19904–19911. [CrossRef]
20. Chen, T.-B.; Rabiee, H.; Yan, P.; Zhu, Z.; Ge, L. Enhancing the Ammonia Catalytic Decomposition of Lanthanum Strontium Titanate Nickel Perovskite Catalysts via a Balanced Cation Doping and Deficiency Strategy. *Energy Fuels* **2024**, *38*, 5449–5456. [CrossRef]
21. Maleki, H.; Bertola, V. Co–Ce–Al–O mesoporous catalysts for hydrogen generation via ammonia decomposition. *Int. J. Hydrogen Energy* **2024**, *51*, 267–275. [CrossRef]
22. Im, Y.; Muroyama, H.; Matsui, T.; Eguchi, K. Ammonia decomposition over nickel catalysts supported on alkaline earth metal aluminate for H_2 production. *Int. J. Hydrogen Energy* **2020**, *45*, 26979–26988. [CrossRef]
23. Alamoudi, M.A.; Podila, S. Role of Perovskite Phase in $CeXO_3$ (X = Ni, Co, Fe) Catalysts for Low-Temperature Hydrogen Production from Ammonia. *Catalysts* **2025**, *15*, 1079. [CrossRef]
24. Kowalczyk, A.; Zaryczny, M.; Piwowarska, Z.; Chmielarz, L. Ni-Mg-Al Hydrotalcite-Derived Catalysts for Ammonia Decomposition—From Precursor to Effective Catalyst. *Molecules* **2025**, *30*, 1052. [CrossRef] [PubMed]
25. Kowalczyk, A.; Rutkowska, M.; Gnyla, S.; Pacia, M.; Chmielarz, L. Synergistic Effect of Co and Ni Co-Existence on Catalytic Decomposition of Ammonia to Hydrogen—Effect of Catalytic Support and Mg-Al Oxide Matrix. *ChemEngineering* **2024**, *8*, 55. [CrossRef]
26. Zhao, X.; Teng, Q.; Tao, H.; Tang, W.; Chen, Y.; Zhou, B.; Sang, J.; Huang, S.; Guan, W.; Li, H.; et al. FeCo Alloy-Decorated Proton-Conducting Perovskite Oxide as an Efficient and Low-Cost Ammonia Decomposition Catalyst. *Catalysts* **2024**, *14*, 850. [CrossRef]
27. Sima, D.; Wu, H.; Tian, K.; Xie, S.; Foo, J.J.; Li, S.; Wang, D.; Ye, Y.; Zheng, Z.; Liu, Y.-Q. Enhanced low temperature catalytic activity of Ni/Al–$Ce_{0.8}Zr_{0.2}O_2$ for hydrogen production from ammonia decomposition. *Int. J. Hydrogen Energy* **2020**, *45*, 9342–9352. [CrossRef]
28. Rajkumar, T.; Sápi, A.; Ábel, M.; Farkas, F.; Gómez-Pérez, J.F.; Kukovecz, Á.; Kónya, Z. Ni–Zn–Al-Based Oxide/Spinel Nanostructures for High Performance, Methane-Selective CO_2 Hydrogenation Reactions. *Catal. Lett.* **2020**, *150*, 1527–1536. [CrossRef]
29. Lv, Y.; Yan, H.; Liu, T.; Xu, J.; Xu, X.; Fang, X.; Wang, X. Manufacturing AAl_2O_4 (A=Cu, Co, Ni, Zn) Spinel Catalysts for Toluene Combustion: Elucidating the A-site Replacement Effect on the Reactivity. *ChemCatChem* **2024**, *16*, e202301264. [CrossRef]
30. Tangcharoen, T.; T-Thienprasert, J.; Kongmark, C. Optical properties and versatile photocatalytic degradation ability of MAl_2O_4 (M = Ni, Cu, Zn) aluminate spinel nanoparticles. *J. Mater. Sci. Mater. Electron.* **2018**, *29*, 8995–9006. [CrossRef]
31. Tangcharoen, T.; T-Thienprasert, J.; Kongmark, C. Effect of calcination temperature on structural and optical properties of MAl_2O_4 (M = Ni, Cu, Zn) aluminate spinel nanoparticles. *J. Adv. Ceram.* **2019**, *8*, 352–366. [CrossRef]
32. Ragupathi, C.; Vijaya, J.J.; Kennedy, L.J. Preparation, characterization and catalytic properties of nickel aluminate nanoparticles: A comparison between conventional and microwave method. *J. Saudi Chem. Soc.* **2017**, *21*, S231–S239. [CrossRef]
33. Mahmoud, S.A.; Elsisi, M.E.; Mansour, A.F. Synthesis and electrochemical performance of α-Al_2O_3 and M-Al_2O_4 spinel nanocomposites in hybrid quantum dot-sensitized solar cells. *Sci. Rep.* **2022**, *12*, 17009. [CrossRef] [PubMed]
34. Sun, Y.; Jiang, E.; Xu, X.; Wang, J.; Li, Z. Supplied Oxygen Properties of NiO/$NiAl_2O_4$ in Chemical Looping Re-Forming of Biomass Pyrolysis Gas: The Influence of Synthesis Method. *ACS Sustain. Chem. Eng.* **2018**, *6*, 14660–14668. [CrossRef]
35. Guo, S.; Zhang, L.; Chen, M.; Ahmad, F.; Fida, H.; Zhang, H. Heterogeneous Activation of Peroxymonosulfate by a Spinel $CoAl_2O_4$ Catalyst for the Degradation of Organic Pollutants. *Catalysts* **2022**, *12*, 847. [CrossRef]
36. Sun, Q.; Zhao, J.; Hu, Z.; Zhang, J.; Yan, J.; Sheng, J. Novel fabrication of rod-like $CoAl_2O_4$/halloysite hybrid pigment derived from Co-MOF/nano-clay and mechanism exploration. *Dye. Pigment.* **2022**, *201*, 110216. [CrossRef]

37. He, K.; Yang, Y.; Zhao, Z.; Yan, Z.; Xiao, X. One-Step Synthesis $AlCo_2O_4$ and Derived "Al" to Double Optimise the Thermal Decomposition Kinetics and Enthalpy of Ammonium Perchlorate. *Colloids Interfaces* **2025**, *9*, 28. [CrossRef]
38. Betancur Granados, N.; Yi, E.; Restrepo, O. $CoAl_2O_4$ blue nanopigments prepared by liquid-feed flame spray pyrolysis method. *Matéria* **2015**, *20*, 580–587. [CrossRef]
39. Zhao, X.Q.; Veintemillas-Verdaguer, S.; Bomati-Miguel, O.; Morales, M.P.; Xu, H.B. Thermal history dependence of the crystal structure of Co fine particles. *Phys. Rev. B* **2005**, *71*, 024106. [CrossRef]
40. Guo, Q.; Guo, X.; Tian, Q. Optionally ultra-fast synthesis of CoO/Co_3O_4 particles using $CoCl_2$ solution via a versatile spray roasting method. *Adv. Powder Technol.* **2010**, *21*, 529–533. [CrossRef]
41. Prasanth, G.; Madhu, G.M.; Kottam, N. $CeAlO_3$ nanoparticle synthesis through combustion-assisted method and structural property assessment in Nano-$CeAlO_3$ polymer composites. *Mater. Technol.* **2024**, *39*, 2330279. [CrossRef]
42. Zheng, X.; Qi, J.; Zheng, Y.; Liu, C. Synthesis and characterization of $CeAlO_3$ via solid state method. *J. Solid State Chem.* **2022**, *312*, 123220. [CrossRef]
43. Vasylkovskyi, V.; Bespalova, I.; Gryshkov, O.; Slipchenko, M.; Tkachenko, S.; Arhipov, P.; Gerasymov, I.; Zholudov, Y.; Zhao, Z.; Feldhoff, A.; et al. Laser generation of $CeAlO_3$ nanocrystals with perovskite structure. *Appl. Phys. A* **2023**, *129*, 714. [CrossRef]
44. Ma, Y.; Ma, Y.; Li, J.; Li, Q.; Hu, X.; Ye, Z.; Wu, X.-Y.; Buckley, C.E.; Dong, D. CeO_2-promotion of $NiAl_2O_4$ reduction via $CeAlO_3$ formation for efficient methane reforming. *J. Energy Inst.* **2020**, *93*, 991–999. [CrossRef]
45. Dhrithi, H.R.; Rajaji, U.; Hung, K.-Y.; Swamy, B.E.K.; Habila, M. Designing of cerium aluminum trioxide intercalated with functionalized carbon nanofibers-based electrochemical sensor for mercury (II) ions detection in environmental water samples. *J. Environ. Chem. Eng.* **2026**, *14*, 121762. [CrossRef]
46. Harish, B.M.; Yallappa, S.; Avinash, B.S.; Chaturmukha, V.S.; Jayanna, H.S.; Lamani, A.R. Temperature Dependent Dielectric Constant and AC Conductivity of Porous CeO_2 Nanoparticles Obtained by Solution Combustion Method. *J. Nanofluids* **2018**, *7*, 620–625. [CrossRef]
47. Charif, M.L.; Doukeh, R.; Ciuparu, D.M. The Catalytic Performance of Metal-Oxide-Based Catalysts in the Synthesis of Glycerol Carbonate: Toward the Green Valorization of Glycerol. *Catalysts* **2025**, *15*, 534. [CrossRef]
48. Charif, M.L.; Ciuparu, D.M.; Lixandru Matei, I.L.; Vasilievici, G.; Banu, I.; Băjan, M.; Bomboș, D.; Dușescu-Vasile, C.; Ghețiu, I.V.; Panaitescu, C.; et al. An Experimental Study of Glycerol Carbonate Synthesis over g-C_3N_4 Catalysts. *Appl. Sci.* **2025**, *15*, 6236. [CrossRef]
49. Doukeh, R.; Eparu, C.N.; Prundurel, A.P.; Tudose, M.; Brănoiu, G.; Ghețiu, I.V.; Păun, L.Ș.; Mihai, S.; Stan, I.G.; Stoica, D.B. Synthesis, Characterization, and Performance Evaluation of Nanocrystalline Metal Oxides for Shale Inhibition in Water-Based Drilling Fluids. *Sustain. Chem.* **2026**, *7*, 3. [CrossRef]
50. Wang, J.; Wang, X.; Zhou, P.; Bian, L.; Wang, F. A Simple Fabrication of Tourmaline-Supported Ni-$NiAl_2O_4$ Nanocomposites for Enhanced Methane Dry Reforming Activity. *Catalysts* **2025**, *15*, 658. [CrossRef]
51. Samikannu, P.; Madhan, V.; Chiang, K.-Y.; George, R.K.; Ravi, R. Polylactic acid-based plastic activated $NiAl_2O_4$ nanoparticles as highly active positive electrode materials for energy storage supercapacitor. *Environ. Sci. Pollut. Res.* **2024**, *31*, 26606–26617. [CrossRef]
52. Kien, N.T.; Lam, V.D.; Duong, P.V.; Hien, N.T.; Luyen, N.T.; Do, P.V.; Binh, N.T.; Ca, N.X. New insights on the optical properties and upconversion fluorescence of Er-doped $CoAl_2O_4$ nanocrystals. *RSC Adv.* **2024**, *14*, 3712–3722. [CrossRef]
53. Panda, P.; Mishra, R.; Panigrahy, S.; Barman, S. 3D Assembly of $CoAl_2O_4$ Spinel Nanosheets for Energy Storage. *ACS Appl. Nano Mater.* **2022**, *5*, 5176–5186. [CrossRef]
54. Sheng, Z.; Gafurovih, K.F.; Raimovna, K.Z.; Gao, B.; Mao, L. Sustainable recovery of nickel and aluminum from spent $NiAl_2O_4$ catalysts via soda roasting-water leaching: Disruption of $NiAl_2O_4$ and leaching kinetic. *Chemosphere* **2025**, *387*, 144668. [CrossRef]
55. Kamonsuangkasem, K.; Therdthianwong, S.; Therdthianwong, A.; Thammajak, N. Remarkable activity and stability of Ni catalyst supported on CeO_2-Al_2O_3 via $CeAlO_3$ perovskite towards glycerol steam reforming for hydrogen production. *Appl. Catal. B Environ.* **2017**, *218*, 650–663. [CrossRef]
56. Zhang, L.; Wang, X.; Chen, C.; Zou, X.; Shang, X.; Ding, W.; Lu, X. Investigation of mesoporous $NiAl_2O_4$/MOx (M = La, Ce, Ca, Mg)–γ-Al_2O_3 nanocomposites for dry reforming of methane. *RSC Adv.* **2017**, *7*, 33143–33154. [CrossRef]
57. Bui, H.M.; Kratky, T.; Lee, I.; Khare, R.; Hiller, M.; Wedig, S.; Günther, S.; Hinrichsen, O. In situ impregnated Ni/Al_2O_3 catalysts prepared by binder jet 3D printing using nickel nitrate-containing ink. *Catal. Commun.* **2023**, *182*, 106738. [CrossRef]
58. Duan, X.; Pan, M.; Yu, F.; Yuan, D. Synthesis, structure and optical properties of $CoAl_2O_4$ spinel nanocrystals. *J. Alloys Compd.* **2011**, *509*, 1079–1083. [CrossRef]
59. Bensemmane, N.; Medjadji, H.; Salhi, N.; Boulahouache, A.; Derkaoui, K.; Skender, A. Sol–Gel Derived $CoAl_2O_4$ Sheets: Synthesis, Characterization, and Photocatalytic Efficiency for Methylene Blue Degradation under Visible Light. *ChemistrySelect* **2025**, *10*, e02310. [CrossRef]
60. Castle, J.E. Practical surface analysis by Auger and X-ray photoelectron spectroscopy. D. Briggs and M. P. Seah (Editors). John Wiley and Sons Ltd, Chichester, 1983, 533 pp., £44.50. *Surf. Interface Anal.* **1984**, *6*, 302. [CrossRef]

61. Tian, C.; Yuan, L.; Wen, T.; Jin, E.; Jia, D.; Yu, J. Direct synthesis of $CeAlO_3$ by carbon-bed method under high temperature. *Ceram. Int.* **2020**, *46*, 7871–7878. [CrossRef]
62. Prakash, A.S.; Shivakumara, C.; Hegde, M.S. Single step preparation of $CeO_2/CeAlO_3/\gamma$-Al_2O_3 by solution combustion method: Phase evolution, thermal stability and surface modification. *Mater. Sci. Eng. B* **2007**, *139*, 55–61. [CrossRef]
63. Ghemit, K.; Akika, F.Z.; Rouibah, K.; Benamira, M.; Bousba, D.; Gouasmia, A.; Djermoune, A.; Oueslati, A.; Avramova, I. Photocatalytic activity of the new $NiAl_2O_4/CeO_2$ heterojunction for the elimination of Rose Bengal under solar irradiation. *Inorg. Chem. Commun.* **2025**, *176*, 114185. [CrossRef]
64. Dupin, J.-C.; Gonbeau, D.; Vinatier, P.; Levasseur, A. Systematic XPS studies of metal oxides, hydroxides and peroxides. *Phys. Chem. Chem. Phys.* **2000**, *2*, 1319–1324. [CrossRef]
65. Biesinger, M.C.; Payne, B.P.; Grosvenor, A.P.; Lau, L.W.M.; Gerson, A.R.; Smart, R.S.C. Resolving surface chemical states in XPS analysis of first row transition metals, oxides and hydroxides: Cr, Mn, Fe, Co and Ni. *Appl. Surf. Sci.* **2011**, *257*, 2717–2730. [CrossRef]
66. Kim, J.G.; Pugmire, D.L.; Battaglia, D.; Langell, M.A. Analysis of the $NiCo_2O_4$ spinel surface with Auger and X-ray photoelectron spectroscopy. *Appl. Surf. Sci.* **2000**, *165*, 70–84. [CrossRef]
67. Platero, E.E.; Arean, C.O.; Parra, J.B. Synthesis of high surface area $CoAl_2O_4$ and $NiAl_2O_4$ spinels by an alkoxide route. *Res. Chem. Intermed.* **1999**, *25*, 187–194. [CrossRef]
68. Bêche, E.; Charvin, P.; Perarnau, D.; Abanades, S.; Flamant, G. Ce 3d XPS investigation of cerium oxides and mixed cerium oxide (CexTiyOz). *Surf. Interface Anal.* **2008**, *40*, 264–267. [CrossRef]
69. Isaacs, M.A.; Drivas, C.; Lee, R.; Palgrave, R.; Parlett, C.M.A.; Morgan, D.J. XPS surface analysis of ceria-based materials: Experimental methods and considerations. *Appl. Surf. Sci. Adv.* **2023**, *18*, 100469. [CrossRef]
70. Paparazzo, E. Use and mis-use of x-ray photoemission spectroscopy Ce3d spectra of Ce_2O_3 and CeO_2. *J. Phys. Condens. Matter* **2018**, *30*, 343003. [CrossRef]
71. Pireaux, J.J.; Riga, J.; Thibaut, E.; Tenret-Noël, C.; Caudano, R.; Verbist, J.J. Shake-up satellites in the x-ray photoelectron spectra of uranium oxides and fluorides. A band structure scheme for uranium dioxide, UO_2. *Chem. Phys.* **1977**, *22*, 113–120. [CrossRef]
72. van den Brand, J.; Snijders, P.C.; Sloof, W.G.; Terryn, H.; de Wit, J.H.W. Acid−Base Characterization of Aluminum Oxide Surfaces with XPS. *J. Phys. Chem. B* **2004**, *108*, 6017–6024. [CrossRef]
73. Cañón, J.; Teplyakov, A.V. XPS characterization of cobalt impregnated SiO_2 and γ-Al_2O_3. *Surf. Interface Anal.* **2021**, *53*, 475–481. [CrossRef]
74. Wang, X.; Liu, Y.; Zhang, T.; Luo, Y.; Lan, Z.; Zhang, K.; Zuo, J.; Jiang, L.; Wang, R. Geometrical-Site-Dependent Catalytic Activity of Ordered Mesoporous Co-Based Spinel for Benzene Oxidation: In Situ DRIFTS Study Coupled with Raman and XAFS Spectroscopy. *ACS Catal.* **2017**, *7*, 1626–1636. [CrossRef]
75. Ming, H.; Baker, B.G.; Jasieniak, M. Characterization of cobalt Fischer–Tropsch catalysts: 2. Rare earth-promoted cobalt-silica gel catalysts prepared by wet impregnation. *Appl. Catal. A Gen.* **2010**, *381*, 216–225. [CrossRef]
76. Ji, L.; Tang, S.; Zeng, H.C.; Lin, J.; Tan, K.L. CO_2 reforming of methane to synthesis gas over sol–gel-made Co/γ-Al_2O_3 catalysts from organometallic precursors. *Appl. Catal. A Gen.* **2001**, *207*, 247–255. [CrossRef]
77. Thommes, M.; Kaneko, K.; Neimark, A.V.; Olivier, J.P.; Rodriguez-Reinoso, F.; Rouquerol, J.; Sing, K.S.W. Physisorption of gases, with special reference to the evaluation of surface area and pore size distribution (IUPAC Technical Report). *Pure Appl. Chem.* **2015**, *87*, 1051–1069. [CrossRef]
78. Chen, K.; Zhang, T.; Chen, X.; He, Y.; Liang, X. Model construction of micro-pores in shale: A case study of Silurian Longmaxi Formation shale in Dianqianbei area, SW China. *Pet. Explor. Dev.* **2018**, *45*, 412–421. [CrossRef]
79. Stawowy, M.; Róziewicz, M.; Szczepańska, E.; Silvestre-Albero, J.; Zawadzki, M.; Musioł, M.; Łuzny, R.; Kaczmarczyk, J.; Trawczyński, J.; Łamacz, A. The Impact of Synthesis Method on the Properties and CO_2 Sorption Capacity of UiO-66(Ce). *Catalysts* **2019**, *9*, 309. [CrossRef]
80. Chernykh, M.; Mikheeva, N.; Zaikovskii, V.; Salaev, M.; Liotta, L.F.; Mamontov, G. Room-Temperature Nitrophenol Reduction over Ag–CeO_2 Catalysts: The Role of Catalyst Preparation Method. *Catalysts* **2020**, *10*, 580. [CrossRef]
81. Busca, G. The surface of transitional aluminas: A critical review. *Catal. Today* **2014**, *226*, 2–13. [CrossRef]
82. Unger, K.K. (Ed.) Chapter 3 Surface chemistry of porous silica. In *Journal of Chromatography Library*; Elsevier: Amsterdam, The Netherlands, 1979; Volume 16, pp. 57–146.
83. Doukeh, R.; Joe, A.-C.; Onuțu, I.; Ghețiu, I.V.; Băjan, M.; Vasilievici, G.; Bomboș, D.; Baioun, A.; Panaitescu, C.; Banu, I.; et al. A Glycerol Acetylation Study on a Tin Ferrite Nanocatalyst. *ChemEngineering* **2025**, *9*, 86. [CrossRef]
84. Yazıcı, D.; Bilgiç, C. Determining the surface acidic properties of solid catalysts by amine titration using Hammett indicators and FTIR-pyridine adsorption methods. *Surf. Interface Anal.* **2010**, *42*, 959–962. [CrossRef]
85. Barzetti, T.; Selli, E.; Moscotti, D.; Forni, L. Pyridine and ammonia as probes for FTIR analysis of solid acid catalysts. *J. Chem. Soc. Faraday Trans.* **1996**, *92*, 1401–1407. [CrossRef]

86. Doukeh, R.; Râpă, M.; Matei, E.; Prodan, D.; Győrgy, R.; Trifoi, A.; Banu, I. An Evaluation of Glycerol Acetalization with Benzaldehyde over a Ferromagnetic Heteropolyacid Catalyst. *Catalysts* **2023**, *13*, 782. [CrossRef]
87. Xiao, H.; Zhang, J.; Wang, P.; Zhang, Z.; Zhang, Q.; Xie, H.; Yang, G.; Han, Y.; Tan, Y. Mechanistic insight to acidity effects of Ga/HZSM-5 on its activity for propane aromatization. *RSC Adv.* **2015**, *5*, 92222–92233. [CrossRef]
88. Doukeh, R.; Bombos, D.; Bombos, M.; Oprescu, E.-E.; Dumitrascu, G.; Vasilievici, G.; Calin, C. Catalytic hydrotreating of bio-oil and evaluation of main noxious emissions of gaseous phase. *Sci. Rep.* **2021**, *11*, 6176. [CrossRef]
89. Emeis, C.A. Determination of Integrated Molar Extinction Coefficients for Infrared Absorption Bands of Pyridine Adsorbed on Solid Acid Catalysts. *J. Catal.* **1993**, *141*, 347–354. [CrossRef]
90. Hao, S.; Ding, C.; Wang, T.; Zheng, S.; Wang, Z. Fe-Co/Al-CeZr-M multi-shelled nanosphere catalysts derived from self-templated synthesis for hydrogen production by ammonia decomposition. *Fuel* **2025**, *397*, 135425. [CrossRef]
91. Zhao, Z.; Liu, Z.; Li, M.; Yang, Y.; Deng, L.; Zhao, Y.; Dou, B.; Bin, F. Enhancing ammonia decomposition for hydrogen production via optimization of interface effects and acidic site in supported cobalt-nickel alloy catalysts. *Sep. Purif. Technol.* **2025**, *360*, 131144. [CrossRef]
92. Yan, Z.; Fan, J.; Zuo, Z.; Li, Z.; Zhang, J. NH_3 adsorption on the Lewis and Bronsted acid sites of MoO_3 (010) surface: A cluster DFT study. *Appl. Surf. Sci.* **2014**, *288*, 690–694. [CrossRef]
93. Guo, W.; Vlachos, D.G. Patched bimetallic surfaces are active catalysts for ammonia decomposition. *Nat. Commun.* **2015**, *6*, 8619. [CrossRef]
94. Simonsen, S.B.; Chakraborty, D.; Chorkendorff, I.; Dahl, S. Alloyed Ni-Fe nanoparticles as catalysts for NH_3 decomposition. *Appl. Catal. A Gen.* **2012**, *447–448*, 22–31. [CrossRef]
95. Mizoguchi, H.; Luo, S.; Sasase, M.; Kitano, M.; Hosono, H. Ammonia Decomposition Catalyzed by Co Nanoparticles Encapsulated in Rare Earth Oxide. *J. Phys. Chem. Lett.* **2025**, *16*, 796–801. [CrossRef] [PubMed]
96. Cheddie, D.F. Temkin-Pyzhev Kinetics in Intermediate Temperature Ammonia-Fed Solid Oxide Fuel Cells (SOFCs). *Int. J. Power Energy Res.* **2018**, *2*, 43–51. [CrossRef]
97. Almisbaa, Z.; Sautet, P. Ba promoter effect on cobalt-catalyzed ammonia decomposition kinetics: A theoretical analysis. *J. Energy Chem.* **2024**, *99*, 182–192. [CrossRef]
98. Lucentini, I.; García Colli, G.; Luzi, C.D.; Serrano, I.; Martínez, O.M.; Llorca, J. Catalytic ammonia decomposition over Ni-Ru supported on CeO_2 for hydrogen production: Effect of metal loading and kinetic analysis. *Appl. Catal. B Environ.* **2021**, *286*, 119896. [CrossRef]
99. Rossetti, I.; Pernicone, N.; Ferrero, F.; Forni, L. Kinetic Study of Ammonia Synthesis on a Promoted Ru/C Catalyst. *Ind. Eng. Chem. Res.* **2006**, *45*, 4150–4155. [CrossRef]
100. Lucentini, I.; Garcia, X.; Vendrell, X.; Llorca, J. Review of the Decomposition of Ammonia to Generate Hydrogen. *Ind. Eng. Chem. Res.* **2021**, *60*, 18560–18611. [CrossRef]
101. Armenise, S.; García-Bordejé, E.; Valverde, J.L.; Romeo, E.; Monzón, A. A Langmuir–Hinshelwood approach to the kinetic modelling of catalytic ammonia decomposition in an integral reactor. *Phys. Chem. Chem. Phys.* **2013**, *15*, 12104–12117. [CrossRef]
102. Itoh, N.; Oshima, A.; Suga, E.; Sato, T. Kinetic enhancement of ammonia decomposition as a chemical hydrogen carrier in palladium membrane reactor. *Catal. Today* **2014**, *236*, 70–76. [CrossRef]
103. Coelho, S.; Matos, J.; Rocha, C.; Soria, M.A.; Madeira, L.M. Hydrogen production via ammonia decomposition: Kinetic analysis. *Chem. Eng. Res. Des.* **2025**, *221*, 328–338. [CrossRef]
104. Lundin, S.-T.B.; Movick, W.J.; Ikeda, A.; Hasegawa, Y.; Wolden, C.A.; Way, J.D. Modeling of an ammonia decomposition membrane reactor including purity with complex geometry and non-isothermal behavior. *J. Membr. Sci.* **2024**, *693*, 122345. [CrossRef]
105. Sayas, S.; Morlanés, N.; Katikaneni, S.P.; Harale, A.; Solami, B.; Gascon, J. High pressure ammonia decomposition on Ru–K/CaO catalysts. *Catal. Sci. Technol.* **2020**, *10*, 5027–5035. [CrossRef]
106. Vasilievici, G.; Sanda, M.; Băjan, M.; Dușescu-Vasile, C.; Onuțu, I.; Brănoiu, G.; Bomboș, D.; Baioun, A.; Borcea, A.F.; Stănică, A.-I. Synthesis and Characterization of Biochar Obtained by Partial Delignification of Waste Biomass. *Molecules* **2025**, *30*, 4505. [CrossRef]

Disclaimer/Publisher's Note: The statements, opinions and data contained in all publications are solely those of the individual author(s) and contributor(s) and not of MDPI and/or the editor(s). MDPI and/or the editor(s) disclaim responsibility for any injury to people or property resulting from any ideas, methods, instructions or products referred to in the content.